





mTORC2 Inhibition Improves Morphological Effects of PTEN Loss, But Does Not Correct Synaptic Dysfunction or Prevent Seizures

 Erin R. Cullen,¹  Kamran Tariq,² Amy N. Shore,^{1,3}  Bryan W. Luikart,² and  Matthew C. Weston^{1,3,4}

¹Department of Neurological Sciences, Larner College of Medicine, University of Vermont, Burlington, Vermont 05405, ²Department of Molecular and Systems Biology, Geisel School of Medicine, Dartmouth College, Hanover, New Hampshire 03755, ³Fralin Biomedical Research Institute at Virginia Tech Carilion, Roanoke, Virginia 24016, and ⁴School of Neuroscience, Virginia Polytechnic and State University, Blacksburg, Virginia 24061

Hyperactivation of PI3K/PTEN-mTOR signaling during neural development is associated with focal cortical dysplasia (FCD), autism, and epilepsy. mTOR can signal through two major hubs, mTORC1 and mTORC2, both of which are hyperactive following PTEN loss of function (LOF). Here, we tested the hypothesis that genetic inactivation of the mTORC2 complex via deletion of *Rictor* is sufficient to rescue morphologic and electrophysiological abnormalities in the dentate gyrus caused by PTEN loss, as well as generalized seizures. An established, early postnatal mouse model of PTEN loss in male and female mice showed spontaneous seizures that were not prevented by mTORC2 inactivation. This lack of rescue occurred despite the normalization or amelioration of many morphologic and electrophysiological phenotypes. However, increased excitatory connectivity proximal to dentate gyrus granule neuron somas was not normalized by mTORC2 inactivation. Further studies demonstrated that, although mTORC2 inactivation largely rescued the dendritic arbor overgrowth caused by PTEN LOF, it increased synaptic strength and caused additional impairments of presynaptic function. These results suggest that a constrained increase in excitatory connectivity and co-occurring synaptic dysfunction is sufficient to generate seizures downstream of PTEN LOF, even in the absence of characteristic changes in morphologic properties.

Key words: dentate gyrus; epilepsy; mTOR; mTORC1; mTORC2; synaptic transmission

Significance Statement

Homozygous deletion of the *Pten* gene in neuronal subpopulations in the mouse serves as a valuable model of epilepsy caused by mTOR hyperactivation. To better understand the physiological mechanisms downstream of *Pten* loss that cause epilepsy, as well as the therapeutic potential of targeted gene therapies, we tested whether genetic inactivation of the mTORC2 complex could improve the cellular, synaptic, and *in vivo* effects of *Pten* loss in the dentate gyrus. We found that mTORC2 inhibition improved or rescued all morphologic effects of *Pten* loss in the dentate gyrus, but synaptic changes and seizures persisted. These data suggest that synaptic dysfunction can drive epilepsy caused by hyperactivation of PI3K/PTEN-mTOR, and that future therapies should focus on this mechanistic link.

Introduction

Hyperactivation of the mammalian target of rapamycin (mTOR) signaling network, via genetic or environmental insults, underlies several neurologic disorders (Costa-Mattioli and Monteggia, 2013; Wong, 2013; Lipton and Sahin, 2014; Crino, 2016). A uniting feature of these diseases, termed mTORopathies, is increased activity of the RAPTOR-containing mTORC1 complex and increased phosphorylation of its targets (e.g., pS6 and p4EBP) (Liu and Sabatini, 2020). A subset of mTORopathies, however, including those caused by gain-of-function variants in genes encoding PI3K subunits and loss-of-function (LOF) variants in *Pten*, also activate the RICTOR-containing mTORC2 complex (Jansen et al., 2015). Previously, treatment with rapamycin, an acute mTORC1 inhibitor,

Received July 8, 2022; revised Nov. 29, 2022; accepted Dec. 12, 2022.

Author contributions: E.R.C., K.T., A.N.S., B.W.L., and M.C.W. designed research; E.R.C., K.T., A.N.S., B.W.L., and M.C.W. performed research; E.R.C., K.T., B.W.L., and M.C.W. analyzed data; E.R.C. wrote the first draft of the paper; E.R.C., K.T., B.W.L., and M.C.W. wrote the paper; A.N.S. and M.C.W. edited the paper.

This work was supported by Autism Speaks Predoctoral Grant 11857 to K.T.; National Institutes of Health Grant R01 MH097949 to B.W.L. and Grant R01 NS110945 to M.C.W.; and COBRE Grant P20GM135007 to the Customized Physiology and Imaging Core at UVM.

The authors declare no competing financial interests.

Correspondence should be addressed to Bryan W. Luikart at bryan.w.luikart@dartmouth.edu or Matthew C. Weston at matthew.c.weston@med.uvm.edu.

<https://doi.org/10.1523/JNEUROSCI.1354-22.2022>

Copyright © 2023 the authors

was shown to improve the cellular, biochemical, and *in vivo* abnormalities in PTEN LOF mouse models, suggesting that mTORC1 hyperactivation mediates the phenotypes of PTEN LOF (Ljungberg et al., 2009; Zhou et al., 2009; Sunnen et al., 2011; Weston et al., 2012; Xiong et al., 2012; Nguyen et al., 2015; Getz et al., 2016). However, recent evidence suggests that this may be dependent on the ability of long-term rapamycin treatment to inhibit mTORC2 (Sarbasov et al., 2006; Lamming et al., 2012), as inactivation of mTORC2 alone is sufficient to rescue the behavioral and neurophysiological abnormalities associated with PTEN LOF (Chen et al., 2019).

In humans, LOF variants in PTEN cause macrocephaly, autism spectrum disorder, intellectual disability, and, more rarely, epilepsy (Marchese et al., 2014; Jansen et al., 2015; Winden et al., 2018; Koboldt et al., 2021). Despite the availability and success of rapamycin and more recently developed “rapalog” mTOR inhibitors, treating these symptoms remains challenging. mTOR inhibitors can confer severe side effects, particularly during development, and these drugs have thus far not been completely effective in treating seizures or neurocognitive symptoms (French et al., 2016; Srivastava et al., 2022). Because PTEN is a common upstream regulator of both mTOR complexes, these disease phenotypes may be dependent on mTORC1 or mTORC2 activity, which engage largely distinct downstream signaling pathways and have distinct effects on soma size, dendrite growth, and synaptic transmission (Laplante and Sabatini, 2012; Angliker et al., 2015; McCabe et al., 2020). Thus, more precise targeting of mTORC1, mTORC2, or their downstream targets may provide superior relief of seizures and other neurologic symptoms, with fewer side effects (Zhang et al., 2020; Nguyen and Bordey, 2021; Nguyen et al., 2022).

In animal models, PTEN LOF induces a variety of cellular and network changes in neural tissue, including increases in soma size, dendritic arborization, and synaptic transmission, preferentially increasing excitatory connectivity (Backman et al., 2001; Kwon et al., 2001, 2006; Weston et al., 2012, 2014; Williams et al., 2015; Barrows et al., 2017). Studies of the effects of PTEN LOF on dentate granule cells (DGCs), neurons thought to be particularly influential in epilepsy, have corroborated these findings (Luikart et al., 2011b; Pun et al., 2012; Williams et al., 2015; Santos et al., 2017). PTEN LOF increases DGC dendrite length in both the outer molecular layer and inner molecular layer (IML) of the dentate gyrus, and stimulation of this extended dendritic arbor produces hypersynchronous activity in the dentate granule cell layer (GCL) (LaSarge et al., 2016; Santos et al., 2017). PTEN LOF in DGCs also increases excitatory synaptic transmission, including mEPSC amplitude and frequency, as well as evoked EPSC (eEPSC) amplitude (Weston et al., 2012; Williams et al., 2015). Whether these cellular and circuit changes are caused by mTORC1 or mTORC2 hyperactivity, and how they relate to *in vivo* phenotypes, is largely unknown.

Genetic deletion of *Raptor*, essential for mTORC1 formation, or *Rictor*, essential for mTORC2 formation, can isolate signaling through one mTOR complex or the other (Angliker et al., 2015; Chen et al., 2019; McCabe et al., 2020). Experiments using this method have shown that mTORC1 and mTORC2 have distinct effects on soma size, dendrite growth, and synaptic transmission (Laplante and Sabatini, 2012; Angliker et al., 2015; McCabe et al., 2020), and their inhibition can influence the pathology induced by PTEN LOF (Chen et al., 2019). To explore epileptogenic mechanisms downstream of PTEN LOF, we inhibited mTORC1 or mTORC2 activity via genetic deletion of *Raptor* or *Rictor* in a

well-characterized mouse model of *Pten* loss (*Gfap-Cre;Pten^{fl/fl}* mice) that shows seizures and prominent pathology in the dentate gyrus (Backman et al., 2001; Kwon et al., 2001; Ljungberg et al., 2009; Sunnen et al., 2011; Weston et al., 2012; Lugo et al., 2013, 2014; Nguyen et al., 2015; Binder and Lugo, 2017). Although mTORC1 inhibition in these mice caused increased mortality in early adulthood, mTORC2 inhibition normalized many of the morphologic and electrophysiological changes caused by *Pten* loss in the dentate gyrus. It did not, however, prevent spontaneous seizures or protect animals against chemically induced seizures. Cellular-level analyses of morphologic and electrophysiological parameters showed that mTORC2 inhibition protected against cellular overgrowth phenotypes, such as increased soma size, dendritic length, and branching, but did not normalize increases in excitatory synaptic transmission, and caused *de novo* impairments in presynaptic transmission. Thus, synaptic dysregulation may function as a seizure mechanism downstream of PTEN LOF, independently of the typically co-occurring morphologic changes.

Materials and Methods

Animals. The original strain of *Gfap-Cre;Pten* mice used for breeding was heterozygous for the floxed *Pten* allele and homozygous for the *Gfap-Cre* transgene (Backman et al., 2001; Kwon et al., 2001). To generate mice in which Cre recombination could be assessed, a mouse WT for *Pten* and homozygous for the *Gfap-Cre* transgene was crossed to a reporter mouse expressing Cre-dependent tdTomato (The Jackson Laboratory, #024477). To generate experimental animals, *Gfap-Cre;Pten^{fl/+}* mice were crossed to mice that were homozygous floxed at the *Raptor* (The Jackson Laboratory, #013188) or *Rictor* alleles (The Jackson Laboratory, #020649). Resultant F1 animals that were heterozygous at all three alleles (*Gfap-Cre*, floxed *Pten*, and floxed *Raptor* or *Rictor*; referred to as Triple Hets) were crossed to each other to create F2 animals that were homozygous at the floxed *Pten*, heterozygous at the floxed *Raptor* or *Rictor*, and WT at the Cre alleles (referred to as Hom Hets). F2 Hom Hets were crossed to F1 Triple Hets, and the resultant experimental animals of either sex were homozygous at the floxed *Pten*, homozygous or WT at the floxed *Raptor* or *Rictor*, and heterozygous at the *Gfap-Cre* alleles. Control animals were homozygous at the floxed *Pten* allele, homozygous or WT at the floxed *Raptor* or *Rictor* alleles, and WT at both *Gfap-Cre* sites.

Surgeries and EEG recordings. Animals were aged to 6 weeks and then implanted with a wireless EEG monitoring headcap. Animals were anesthetized with 4% isoflurane and arranged on a stereotaxic surgical apparatus with ear bars. Anesthesia was maintained with 1.5%–2.5% isoflurane. The skull surface was exposed and bore holes were made with a 23 G needle at six locations on the skull surface. Screws (3/32 inch; Antrin Miniature Specialties) were inserted into the bore holes, secured with VetBond, and then covered with surgical cement. The screws were attached to a six-pin Millimax strip, which was secured to the skull with additional cement. Animals were administered 5 mg/kg ketoprofen after surgery and allowed to recover for at least 5 d before EEG recording. The surgical protocol was based on guidance provided by Pinnacle Technologies (<https://www.pinnacleet.com>).

After recovery from surgery, implanted animals were fitted with wireless three-channel EEG preamplifiers (Pinnacle Technologies), and EEG signal was recorded at 1024 Hz. EEG recording length was dependent on battery life and, as such, varied from 10 to 105 h; 148–535 h of EEG data were collected for each experimental mouse (Table 1), with the exception of the non-outcrossed *Gfap-Cre;Pten* mice, for which EEG phenotypes have previously been well characterized (Ljungberg et al., 2009; Nguyen et al., 2015). Thus, these mice were each recorded for at least 95 h.

Seizure induction. Picrotoxin powder (Tocris) was dissolved in 100% ethanol to create a 10 mM solution. The picrotoxin solution was diluted 1:5 in PBS, and 5 mg/kg was administered intraperitoneally to each animal. Animals were monitored with EEG and video as well as direct

Table 1. EEG monitoring by group

Genotype	Animal	No. of days (no. of seizures)					Total hours	Total seizures	Seizure rate
		Days (7–8 weeks)	Days (9–10 weeks)	Days (11–12 weeks)	Days (13–14 weeks)	Days (15–16 weeks)			
Pten ^(fl/fl) -Raptor ^(+/+) -Cre(-) Control	1	5.6 (0)	4.4 (0)	0.0	0.0	0.0	239.4	0	0
	2	5.3 (0)	5.2 (0)	3.1 (0)	0.0	2.4 (0)	381.4	0	0
	3	5.0 (0)	4.9 (0)	1.8 (0)	5.0 (0)	2.1 (0)	451.8	0	0
	4	9.6 (0)	6.3 (0)	1.0 (0)	4.8 (0)	0.0	520	0	0
	5	5.8 (0)	4.6 (0)	4.2 (0)	5.5 (0)	0.0	483.9	0	0
Pten ^(fl/fl) -Raptor ^(+/+) -Cre(+)	1	6.7 (0)	2.2 (0)	5.7 (0)	0.9 (0)	0.0	371.5	0	0
	2	3.7 (0)	2.4 (0)	1.2 (0)	2.0 (0)	0.0	223.3	0	0
	3	6.2 (0)	5.9 (0)	9.7 (0)	0.2 (0)	0.0	528.8	0	0
	4	5.5 (0)	5.4 (0)	1.0 (0)	4.0 (0)	6.5 (0)	535.5	0	0
	5	4.8 (4)	1.0 (0)	4.1 (0)	0.0	0.0	235.9	4	0.017
Pten ^(fl/fl) -Rictor ^(+/+) or ^(+/fl) or ^(fl/fl) -Cre(-) Control	1	3.0 (0)	0.0	2.3 (0)	0.0	2.8 (0)	194.5	0	0
	2	3.7 (0)	2.3 (0)	0.0	0.0	2.4 (0)	200.6	0	0
	3	4.7 (0)	3.5 (0)	2.0 (0)	0.0	0.0	245.4	0	0
	4	6.0 (0)	0.2 (0)	0.0	3.1 (0)	0.0	225.6	0	0
	5	5.0 (0)	0.0	1.7 (0)	0.0	2.8 (0)	229.3	0	0
	6	5.2 (0)	5.8 (0)	0.0	2.3 (0)	0.0	318.8	0	0
	7	6.5 (0)	4.1 (0)	0.0	2.9 (0)	0.0	323.5	0	0
Pten ^(fl/fl) -Rictor ^(+/+) -Cre(+)	1	3.3 (0)	3.3 (0)	1.2 (0)	0.0	0.0	188.1	0	0
	2	4.7 (0)	3.2 (0)	0.7 (0)	0.2 (0)	0.0	211.2	0	0
	3	1.0 (0)	3.2 (1)	2.7 (0)	2.5 (2)	0.0	226	3	0.013
	4	7.1 (0)	0.2 (0)	2.2 (0)	4.4 (0)	0.0	334.8	0	0
Pten ^(fl/fl) -Rictor ^(fl/fl) -Cre(+)	1	2.2 (0)	0.0	2.2 (0)	1.8 (0)	0.0	148.5	0	0
	2	0.0	1.3 (1)	5.1 (8)	0.0	0.0	154	9	0.058
	3	1.7 (0)	0.0	3.1 (2)	3.2 (1)	0.0	190	3	0.016
	4	3.4 (0)	6.2 (0)	0.0	0.0	0.0	228.9	0	0
	5	7.0 (0)	6.4 (0)	3.2 (0)	1.1 (0)	1.8 (0)	470.2	0	0
Pten ^(+/+) -Cre(+)	1	0.0	0.0	1.3 (0)	0.0	2.8 (0)	97.3	0	0
	2	3.4 (0)	2.3 (0)	0.0	0.0	0.0	139.1	0	0
Pten ^(fl/fl) -Cre(+)	1	4.0 (8)	0.0	0.0	0.0	0.0	95.3	8	0.084
	2	7.1 (6)	0.1 (0)	0.0	0.0	0.0	172.8	6	0.035

observation for 90 min. During this time, all animals displayed abnormal EEG activity, and most had at least one generalized seizure.

EEG analysis. EEG files were converted from Pinnacle's proprietary format to European Data Format files and imported to MATLAB. A filtering program was constructed to flag traces in which seizures were likely to be occurring based on signal amplitude and line length between data points. All 10 s epochs in which signal amplitude exceeded 400 μ V at two points at least 1 s apart were manually reviewed by a rater blinded to genotype. Traces that showed repetitive, high-amplitude oscillatory activity continuously for a minimum of 10 s and showed corresponding video evidence were marked as seizures. Flagged traces were displayed for the rater to manually mark the beginning and end of each seizure.

For picrotoxin-induced seizures, EEG recording was started within 10 s of picrotoxin injection and continued for at least 90 min. Preictal spike activity was assessed only in the portion of the file before the first generalized seizure (classified using the same criteria as spontaneous seizures). This method was chosen because most animals entered a postictal suppression after seizure, characterized by decreased power and amplitude compared with the baseline signal. Activity in this state was not directly comparable to preictal activity; and because seizure latency varied, we could not compare spike activity between animals at later time points. Therefore, the time period leading up to the first generalized seizure was divided into 30 s traces and displayed for a rater blind to genotype to identify interictal events based on EEG and corresponding video data. Interictal events were identified as an isolated spike, spike-wave complex, or cluster of spikes exceeding 3 \times the amplitude of the baseline signal. The total number of interictal events was compared between groups for the entire period leading up to generalized seizure and for the final 10 min before generalized seizure. A limitation of this method is that we were unable to include the 2 Control animals that did not have a generalized seizure during the 90 min recording period in this analysis.

Retroviral dentate gyrus injections. Pten^(fl/fl);Rictor^(+/+) and Pten^(fl/fl);Rictor^(fl/fl) animals of either sex in a pure C57BL/6J background (The Jackson Laboratory, #006440 and #020649) were injected with retroviral constructs containing GFP with Cre recombinase (Addgene #66693), and mCherry without Cre recombinase (Addgene #66700), which were generated and packaged as previously described (Luikart et al., 2011a; Williams et al., 2015). The detailed method of stereotaxic surgery has also been published previously (Fricano-Kugler et al., 2016). Briefly, iso-flurane-anesthetized pups at P7 were injected with 2 μ l of replication-incompetent retrovirus into the dentate gyrus bilaterally (coordinates relative to λ : $x = \pm 1.3$ mm, $y = 1.55$ mm, $z = -2.3$ to -2.0 mm), at a rate of 0.3 μ l/min with 25% of the virus injected at each z depth.

Slice electrophysiology. Slice electrophysiology was conducted at P20–P30. Animals were deeply anesthetized and decapitated, and the brain was quickly dissected into ice-cold cutting solution (126 mM NaCl, 25 mM NaHCO₃, 10 mM D-glucose, 3.5 mM KCl, 1.5 mM NaH₂PO₄, 0.5 mM CaCl₂, 10.0 mM MgCl₂, pH 7.3–7.4); 350 μ m slices were cut using a Leica 1000S Vibratome. Slices were transferred to 37°C aCSF (126 mM NaCl, 3.5 mM KCl, 1.0 mM MgCl₂, 2.0 mM CaCl₂, 1.5 mM NaH₂PO₄, 25 mM NaHCO₃, and 10 mM D-glucose, pH 7.3–7.4) and incubated for 30 min. The slices were then incubated at room temperature for at least another 30 min before recording. All solutions were continuously bubbled with 95% O₂ and 5% CO₂. Individual slices were transferred to a recording chamber located on an upright microscope (BX51; Olympus) and were perfused with oxygenated aCSF (2 ml/min).

Whole-cell voltage-clamp and current-clamp recordings were obtained using Multiclamp 700B and Clampex 10.5 software (Molecular Devices). Cells in the dentate gyrus GCL were targeted indiscriminately. Intracellular solution contained the following: 136 mM K-gluconate, 17.8 mM HEPES, 1 mM EGTA, 0.6 mM MgCl₂, 4 mM ATP, 0.3 mM GTP, 12 mM creatine phosphate, and 50 U/ml phosphocreatine kinase, pH 7.2. When patch electrodes were filled with intracellular solution, their

resistance ranged from 4 to 6 M Ω . Access resistance was monitored continuously for each cell.

For current-clamp experiments, the intrinsic electrophysiological properties of neurons were tested by injecting 500 ms square current pulses incrementing in 20 pA steps, starting with -100 pA. The membrane time constant was calculated from an exponential fit of current stimulus offset. Input resistance was calculated from the steady state of the voltage responses to the hyperpolarizing current steps. Membrane capacitance was calculated by dividing the time constant by the input resistance. Action potentials (APs) were evoked with 0.5 s, 20 pA depolarizing current steps. Rheobase was defined as the minimum current required to evoke an AP during the 500 ms of sustained somatic current injection. For voltage-clamp experiments to measure sEPSC frequency and amplitude, neurons were held at -70 mV and recorded for 2 min. All electrophysiology data were analyzed offline with AxoGraph X software (AxoGraph Scientific).

Single-neuron culture. Single-neuron primary cultures were grown on astrocytes derived from WT C57BL/6J mice (The Jackson Laboratory, stock #000664), as previously described (Weston et al., 2012, 2014; McCabe et al., 2020). To isolate astrocytes, cortices were dissected from postnatal day 0–1 (P0–P1) pups and placed in 0.05% trypsin-EDTA (Invitrogen) for 15 min at 37°C in a Thermomixer (Eppendorf) with gentle agitation (800 rpm). Then the tissue was mechanically dissociated with a 1 ml pipette tip and the cells were plated into T-75 flasks containing astrocyte media [DMEM media supplemented with glutamine (Invitrogen) and MITO+ Serum Extender (Corning)]. After the astrocytes reached confluency, they were washed with PBS (Invitrogen) and incubated for 5 min in 0.05% trypsin-EDTA at 37°C, and then resuspended in astrocyte media. For conventional cultures, the astrocytes were added to 6-well plates containing 25 mm coverslips pre-coated with coating mixture [0.7 mg/ml collagen I (Corning) and 0.1 mg/ml poly-D-lysine (Sigma) in 10 mM acetic acid]. For single-neuron cultures (Burgalossi et al., 2012), the astrocytes were added to 6-well plates containing 25 mm agarose-coated coverslips stamped with coating mixture using a custom-built stamp to achieve uniformly sized, astrocyte microislands (200 μ m diameter).

To isolate neurons, the hippocampi from P0–P1 *Pten^{fl/fl};Rictor^{+/-}* and *Pten^{fl/fl};Rictor^{fl/fl}* mice of either sex were dissected in cold HBSS (Invitrogen), then digested with papain (Worthington) for 60–75 min, and treated with inactivating solution (Worthington) for 10 min, both while shaking at 800 rpm at 37°C in a Thermomixer. The neurons were then mechanically dissociated and counted. For single-neuron cultures, 2000–3000 neurons/well were added to 6-well plates in NBA plus [Neurobasal-A medium (Invitrogen) supplemented with Glutamax (Invitrogen) and B27 (Invitrogen)], each well containing a 25 mm coverslip with astrocyte microislands. For conventional cultures for immunofluorescence analysis, 150,000 neurons/well were added to 6-well plates in NBA plus, each well containing a 25 mm coverslip with a confluent layer of astrocytes. After plating, $\sim 4 \times 10^{10}$ genome copies (GC) of either AAV8-SYN-mCherry-Cre or AAV8-SYN-mCherry virus (UNC Vector Core) were added to each well.

Single-neuron electrophysiology. Whole-cell recordings were performed with patch-clamp amplifiers (MultiClamp 700B amplifier; Molecular Devices) under the control of Clampex 10.3 or 10.5 (Molecular Devices, pClamp, RRID:SCR_011323). Data were acquired at 10 kHz and low-pass filtered at 4 kHz. The series resistance was compensated at 70%, and only cells with series resistances maintained at <15 M Ω and stable holding currents of <300 pA were analyzed. The pipette resistance was between 2 and 4 M Ω . Standard extracellular solution contained the following (in mM): 140 NaCl, 2.4 KCl, 10 HEPES, 10 glucose, 4 MgCl₂, and 2 CaCl₂ (pH 7.3, 305 mOsm). Internal solution contained the following: 136 mM KCl, 17.8 mM HEPES, 1 mM EGTA, 0.6 mM MgCl₂, 4 mM ATP, 0.3 mM GTP, 12 mM creatine phosphate, and 50 U/ml phosphocreatine kinase. All experiments were performed at room temperature (22°C–23°C). Whole-cell recordings were performed on neurons from control and experimental groups in parallel on the same day (12–14 DIV).

For voltage-clamp experiments, neurons were held at -70 mV unless noted. AP-evoked EPSCs were triggered by a 2 ms somatic depolarization to 0 mV. The shape of the evoked response and the effect of receptor antagonists [3 mM kynurenic acid (Tocris Bioscience)

or 20 μ M bicuculline (Tocris Bioscience)] were analyzed to verify the glutamatergic or GABAergic identities of the neurons. Neurons were stimulated at 0.2 Hz in standard external solution to measure basal-evoked synaptic responses. Electrophysiology data were analyzed offline with AxoGraph X software (AxoGraph Scientific, RRID:SCR_014284). To determine the number of releasable synaptic vesicles (SVs) onto each neuron, we measured the charge transfer of the transient synaptic current induced by a 5 s application of hypertonic sucrose solution directly onto the neuron and then divided the sucrose charge by the charge of the average miniature event onto the same neuron.

Histology and imaging. *Gfap-Cre;Pten* animals were killed by isoflurane overdose followed by transcardial perfusion with 4% PFA. The animals were killed on the same day as picrotoxin-induced seizure induction. Brains were postfixed in 4% PFA for 24 h and then transferred to 30% sucrose for at least 48 h; 40 μ m coronal slices were cut and preserved in a cryoprotectant solution (50% PBS, 30% ethylene glycol, and 20% glycerol). Before staining, slices were washed 3 times with PBS. A fluorescent Nissl stain (Invitrogen N21482, 1:50) was used to assess soma size and dentate gyrus morphology.

After washing, slices were placed in blocking solution (10% normal goat serum, 0.1% Triton X-100, and PBS) for 1 h. Slices were incubated in the following primary antibodies for 3 h at room temperature: pAKT (rabbit polyclonal, 1:1000 dilution, Cell Signaling Technology, catalog #4060), NeuN (guinea pig polyclonal, 1:1000 dilution, Synaptic Systems, catalog #266004), VGLUT1 (rabbit polyclonal, 1:5000 dilution, Synaptic Systems, catalog #135302), and MAP2 (mouse monoclonal, 1:1000 dilution, Synaptic Systems, catalog #188011). Following primary antibody application, slices were washed 3 times in PBS and then incubated in the following AlexaFluor secondary antibodies (Invitrogen) for 1 h at room temperature: goat anti-rabbit 594, goat anti-rabbit 647, goat anti-guinea pig 488, and goat anti-mouse 555.

High-resolution images were acquired using a Nikon C2 confocal microscope (UVM Microscopy Imaging Core). The Nissl-stained slices and pAkt/NeuN-stained slices were imaged with a 10 \times objective and acquired with 2048 \times 2048 resolution and 5 μ m z step. VGLUT1/Map2/NeuN-stained slices were imaged using a 40 \times /1.0 μ m oil immersion lens with 2048 \times 2048 resolution and 2 μ m z step. Z stacks were collapsed into a single image by taking the maximum value of each pixel (mx projected), and the resulting image was used for analysis. Widefield images (2560 \times 2160) were taken with a Zyla sCMOS camera (Andor) mounted on an upright microscope (IX73; Olympus) with a 5 \times objective.

The retrovirally infected animals were anesthetized with Avertin (Sigma Aldrich) and transcardially perfused with 4% PFA in PBS containing 4% sucrose for fixation at P28. The coronal brain slices of 50 μ m (for soma and spine analysis) or 150 μ m (for NeuroLucida) were permeabilized with PBS containing 0.4% Triton-X (PBST) for 30 min and blocked with PBS containing 10% donor horse serum (DHS) for 1 h at room temperature. Sections were incubated with primary antibodies (chicken anti-GFP, 1:3000, Abcam #13970; rabbit anti-mCherry) for 48 h at 4°C in PBS with 2.5% DHS. After three 15 min washes with PBST, sections were incubated for 48 h at 4°C with secondary antibodies (AlexaFluor 488-conjugated goat anti-chicken IgY, Jackson ImmunoResearch Laboratories, #103-545-155; Cy3-conjugated donkey anti-rabbit IgG) at a concentration of 1:200 in PBS containing 2% DHS.

Images were acquired using an LSM510 laser-scanning confocal microscope (Zeiss). For soma size and migration analysis, z stacks of suprapyramidal and infrapyramidal blades of dentate gyrus were acquired at 40 \times /1.3 μ m oil immersion lens with 0.7 \times zoom, at 512 \times 512 resolution with 2 μ m z step. Z stacks of spines were acquired at 63 \times /1.3 μ m-oil immersion lens with 3 \times zoom, at 512 \times 512 resolution with 0.5 μ m z step. For dendritic arbor analysis, images of the 150 μ m dentate gyrus slices were acquired at 20 \times /0.75 μ m plan-apochromat lens with 1 \times zoom, at 512 \times 512 resolution with 2 μ m z step.

Image analysis. For *Gfap-Cre;Pten* animals, image analysis was conducted using ImageJ/Fiji software (National Institutes of Health). Nissl-stained slices were used to assess DGC soma size, GCL width, and lateral

ventricle area. Hippocampal and subcortical landmarks visible on wide-field images were used to confirm that Nissl-stained slices were in equivalent locations (three slices per animal; approximately bregma -1.6 , bregma -2.1 , and bregma -2.6). To measure soma size, $10\times$ images (1 image per slice) were divided into a 10 mm^2 grid formation. All well-defined neuron somas fully within three randomly selected grid squares were manually traced for a total of 20–30 neurons per slice. The average value for each slice was calculated and then averaged by animal; $5\times$ images were used to measure GCL width and lateral ventricle area. To measure GCL width, lines were drawn from the medial to the lateral aspect of the GCL (both the suprapyramidal and infrapyramidal blades) at $\sim 100\text{ }\mu\text{m}$ intervals to capture variation of the width. Both the left and right GCL were measured in each image. Values were averaged within each slice, and slices were averaged by animal. To measure lateral ventricle area, all lateral ventricle boundaries were traced, and the total area was calculated for each image. Slice totals were averaged by animal.

pAkt expression was measured by manually tracing the entire area of the suprapyramidal blade of the dentate gyrus GCL that was present in the image based on NeuN expression (one left-side image and one right-side image per slice; two slices per animal). The mean pixel value of pAkt expression within the entire traced area was calculated, and resulting values were averaged by animal.

VGLUT1 expression was measured by manually tracing the GCL of the suprapyramidal blade of the dentate gyrus based on NeuN expression. The dentate gyrus IML was defined as the region 0–1.0 mm lateral to the traced region. Images were taken at approximately equivalent locations for each animal, and the whole length of the GCL and IML present in the image was analyzed. The mean pixel value within the dentate gyrus GCL and IML was recorded, and the resulting values were averaged by animal. All image analyses were performed while blinded to genotype.

For retrovirally infected DGCs, soma size was quantified by circling somas at maximum circumference using ImageJ/Fiji software (National Institutes of Health) as described previously (Fricano et al., 2014). Migration was expressed as a percentage of GCL traveled, by dividing the distance of soma from hilus boundary by total local GCL width (Getz et al., 2016). Dendritic spine density was quantified with Neuron Studio software (Rodriguez et al., 2008) after deconvolution using ImageJ/Fiji as described previously (Williams et al., 2015). For dendritic arbor analysis, neurons were reconstructed in 3D by user-guided semiautomated tracing in NeuroLucida360 (MBF Biosciences) software. Branched structure and Sholl analysis were performed in NeuroLucida Explorer (MBF Biosciences) software.

Experimental design and statistical analysis. Prism 9 (GraphPad Prism) was used to conduct statistical analyses and create graphs, except where noted otherwise. Log-rank (Mantel–Cox) tests were used for survival analysis and survival curve analysis of induced seizure occurrence and latency (see Figs. 1 and 2). Histologic (see Figs. 1, 3, and 8) electrophysiological (see Fig. 2) comparisons between littermates were analyzed using one-way ANOVA with Tukey *post hoc* analysis. Comparisons between mouse strains were assessed using two-way ANOVA with Tukey *post hoc* (see Fig. 1). Shapiro–Wilk tests were used to test for normality. Kruskal–Wallis tests were substituted when data did not meet criteria for normal distribution (see Figs. 2 and 8). Statistical analysis was performed using a mixed-effects model (Moen et al., 2016) for phenotypes of soma size, migration, and spine and dendritic growth (see Figs. 4 and 5). Two-way ANOVA with Bonferroni's *post hoc* was performed for Sholl analysis. For retrovirus-based morphologic experiments, a mixed-model comparison was made using Stata and *p* values generated using the pwcompare function (Fricano et al., 2014; Moen et al., 2016). To test for statistical significance for whole-cell electrophysiology experiments (see Figs. 6, 7, 9, and 10), we used generalized estimating equations (GEEs) in SPSS (28.0, III, IBM, RRID:SCR_002865), which allows for within-subject correlations and the specification of the most appropriate distribution for the data (McCabe et al., 2021). Because neurons and animals from the same culture or animal are not independent measurements, culture or litter was used as the subject variable, and animals and neurons were considered within-subject measurements. All data distributions were assessed with the Shapiro–Wilk test. Datasets

that were significantly different from the normal distribution ($p < 0.05$) were fit with models using the γ distribution. Normal datasets were fit with models using a linear distribution and identity link. We used the model-based estimator for the covariance matrix, and goodness of fit was determined using the corrected quasi-likelihood under independence model criterion and by the visual assessment of residuals.

Results

Spontaneous seizures in an outbred *Gfap*-driven *Pten* LOF mouse model are not prevented by mTORC2 inactivation

Gfap-Cre;Pten^{fl/fl} mice have spontaneous seizures that are ameliorated by rapamycin treatment (Ljungberg et al., 2009; Sunnen et al., 2011; Nguyen et al., 2015), suggesting that their seizures may also be treatable by inhibiting either mTORC1 or mTORC2. To test whether inactivation of mTORC1 or mTORC2 signaling rescues seizures caused by PTEN LOF, we crossed *Gfap-Cre;Pten^{fl/fl}* mice to *Raptor^{fl/fl}* or *Rictor^{fl/fl}* mice, with the aim of comparing the seizure phenotypes of Cre-negative (Control), *Gfap-Cre;Pten^{fl/fl};Raptor^{+/+}* (Pten LOF), and *Gfap-Cre;Pten^{fl/fl};Raptor^{fl/fl}* (Pten-Raptor LOF) littermates or Cre-negative (Control), *Gfap-Cre;Pten^{fl/fl};Rictor^{+/+}* (Pten LOF), and *Gfap-Cre;Pten^{fl/fl};Rictor^{fl/fl}* (Pten-Rictor LOF) littermates (Fig. 1A).

Two findings of these initial experiments were unexpected. First, Pten-Raptor LOF animals showed increased mortality compared with Control and Pten LOF littermates (Fig. 1B). Of 5 initial Pten-Raptor LOF animals, 1 died before EEG electrode implantation, 2 died during surgery, and 1 died weeks later. Given this high rate of mortality, we focused the remainder of this study on the potential for mTORC2 inhibition to modify PTEN LOF phenotypes using Pten-Rictor LOF animals. Second, Pten LOF progeny resulting from crossing the original *Gfap-Cre;Pten^{fl/fl}* mice (mixed background) to *Raptor^{fl/fl}* or *Rictor^{fl/fl}* mice (C57B6/J background) showed less severe PTEN LOF phenotypes than those of the original parental line (Fig. 1B,C). These phenotypes included *in vivo* (seizure frequency), morphologic (DGC layer width, soma size, and lateral ventricle size, Fig. 1D), and electrophysiological (input resistance and rheobase) measurements, suggesting that the C57B6/J background provided protection against many effects of PTEN LOF.

To test whether mTORC2 inactivation reduces PTEN LOF-induced spontaneous epileptic pathology, we implanted Pten LOF, Pten-Rictor LOF, and Control animals (15 total litters; 1–3 animals per litter) with EEG electrodes at 6 weeks of age and performed chronic video-EEG monitoring of animals beginning 1 week later. Spontaneous generalized seizures were observed in 0 of 12 Control, 2 of 9 Pten LOF, and 2 of 5 Pten-Rictor LOF animals after an average of 302 h of monitoring per animal (range: 148–535 h, Table 1). Electrographic seizures were accompanied by behavioral perturbations, including tail stiffening, behavioral arrest, loss of righting reflex, and clonic movements. Spontaneous seizure frequency and length were not different between Pten LOF and Pten-Rictor LOF animals (Fig. 2A), suggesting that inhibiting mTORC2 activity cannot prevent seizures caused by *Pten* loss in this model.

Gfap-driven *Pten* LOF and Pten-Rictor LOF reduce latency to induced seizure in outbred animals

Because spontaneous generalized seizures were relatively rare in Pten LOF animals, we decided to test whether mTORC2 inactivation affects sensitivity to chemically induced seizures. To do this, we gave an intraperitoneal injection of 5 mg/kg picrotoxin to EEG-implanted animals from the Pten-Rictor LOF line (8

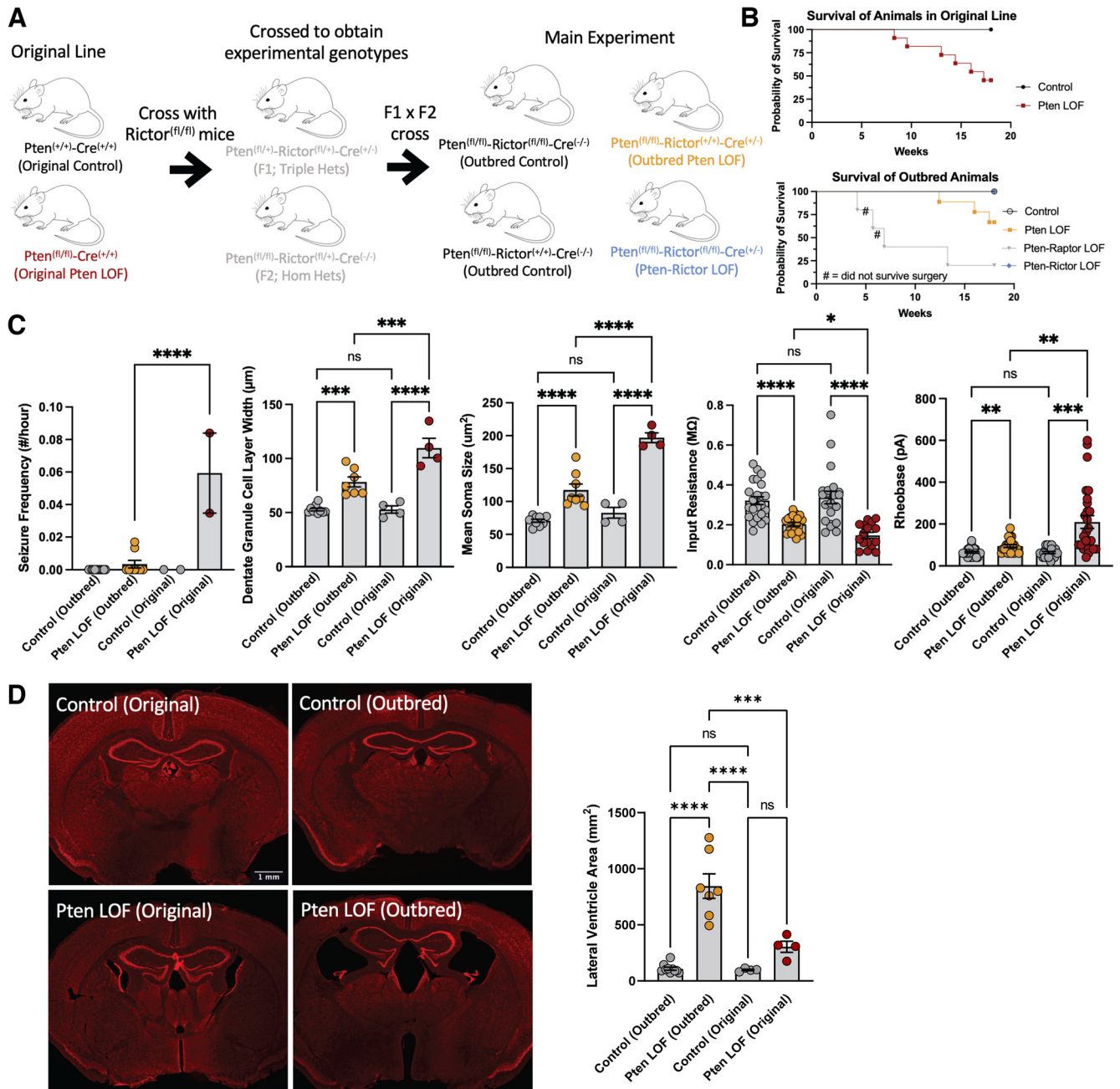


Figure 1. Outbred *GFAP-Cre;Pten* LOF mice have milder cellular perturbations and fewer seizures, but more severely enlarged ventricles. *GFAP-Cre*^(+/+);*Pten*^(fl/fl) mice were crossed to *Rictor*^(fl/fl) mice on a C57BL/6J background, which attenuated the effects of *Pten* loss. **A**, Breeding scheme to generate *Pten* LOF, *Pten*-Rictor LOF, and *Cre*-negative Control mice. **B**, Early mortality occurred in some *Pten* LOF animals in both the original and outbred lines (Original Control vs Original *Pten* LOF $\chi^2 = 7.059$, $p = 0.0070$; Outbred Control vs Outbred *Pten* LOF $\chi^2 = 3.375$, $p = 0.0662$; Original *Pten* LOF vs Outbred *Pten* LOF $\chi^2 = 1.336$, $p = 0.286$). *Pten*-Raptor LOF animals exhibited exacerbated early mortality (Control vs *Pten* LOF $\chi^2 = 3.401$, $p = 0.652$; Control vs *Pten*-Raptor LOF $\chi^2 = 10.82$; $p = 0.0010$; *Pten* LOF vs *Pten*-Raptor LOF $\chi^2 = 5.307$, $p = 0.0212$). **C**, Spontaneous seizure frequency, dentate GCL width, and mean DGC soma size were significantly lower in *Pten* LOF animals in the outbred line than in the original line. DGC input resistance was decreased and rheobase was increased from Control levels in both strains, but these changes were significantly attenuated in outbred *Pten* LOF mice. There were no significant differences between original and outbred Control groups in any of these properties (two-way ANOVA). **D**, Lateral ventricle area was increased from Control levels in outbred *Pten* LOF mice to a greater degree than in *Pten* LOF mice on the original genetic background. Ventricle size significantly differed from Controls in the outbred, but not the original line animals (two-way ANOVA). Error bars indicate mean \pm SEM. ns, $p > 0.05$; * $p < 0.05$; ** $p < 0.01$; *** $p < 0.001$; **** $p < 0.0001$; two-way ANOVA with Tukey multiple comparisons correction.

litters; 1–3 animals per litter) and monitored seizure activity. Most, but not all, animals had at least one generalized seizure within the 90 min recording period after picrotoxin administration (Control: 5 of 7, *Pten* LOF: 4 of 4, *Pten*-Rictor LOF: 5 of 5). The time between picrotoxin administration and the first generalized seizure event in each animal was plotted on a survival curve (Fig. 2B). Among animals that had at least one generalized

seizure, the mean seizure latency was 49.0 ± 10.0 min for Control, 21.5 ± 1.5 min for *Pten* LOF, and 25.2 ± 5.7 min for *Pten*-Rictor LOF animals. The survival curves showed a significant difference between Control and *Pten* LOF animals, and between Control and *Pten*-Rictor LOF animals, but not between *Pten* LOF and *Pten*-Rictor LOF animals. Thus, these data suggest that, in addition to not preventing spontaneous

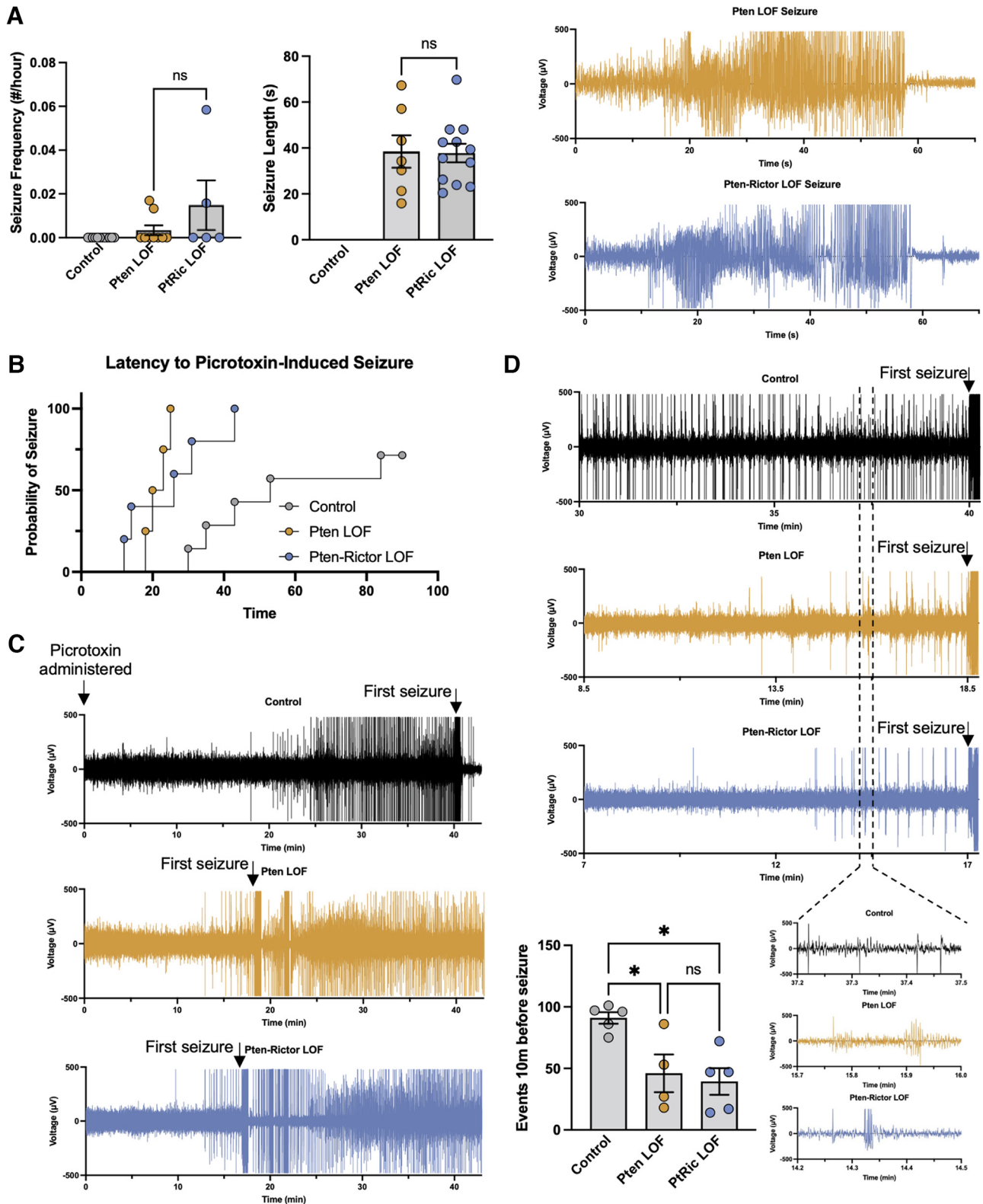


Figure 2. mTORC2 inactivation does not prevent spontaneous seizures or decrease seizure susceptibility in *GFAP-Cre;Pten* LOF mice. **A**, Spontaneous seizures were observed in 2 of 9 Pten LOF and 2 of 5 Pten Rictor LOF animals. There were no significant differences in spontaneous seizure frequency (Kruskal–Wallis test; $K = 4.82$, $p = 0.090$) or length (unpaired t test; $t = 0.096$, $p = 0.925$) between Pten LOF and Pten-Rictor LOF groups. No spontaneous seizures were observed in Control animals. Right, EEG traces demonstrating representative spontaneous generalized seizures. **B**, Latency to induced seizure did not significantly differ between Pten LOF and Pten-Rictor LOF animals ($\chi^2 = 1.254$, $p = 0.263$), but both differed significantly from Control animals (Control vs Pten LOF $\chi^2 = 12.35$, $p = 0.0004$; Control vs Pten-Rictor LOF $\chi^2 = 6.35$, $p = 0.0117$). **C**, EEG traces demonstrating the decreased latency from picrotoxin administration to first seizure in Pten LOF and Pten-Rictor LOF groups. **D**, EEG traces and summary graph showing the decreased number of interictal spike events in the Pten LOF and Pten-Rictor LOF groups compared with that of the Control in the 10 min before induced generalized seizure ($F = 7.625$, $p = 0.008$). Error bars indicate mean \pm SEM. ns, $p > 0.05$; * $p < 0.05$; one-way ANOVA with Tukey multiple comparisons correction.

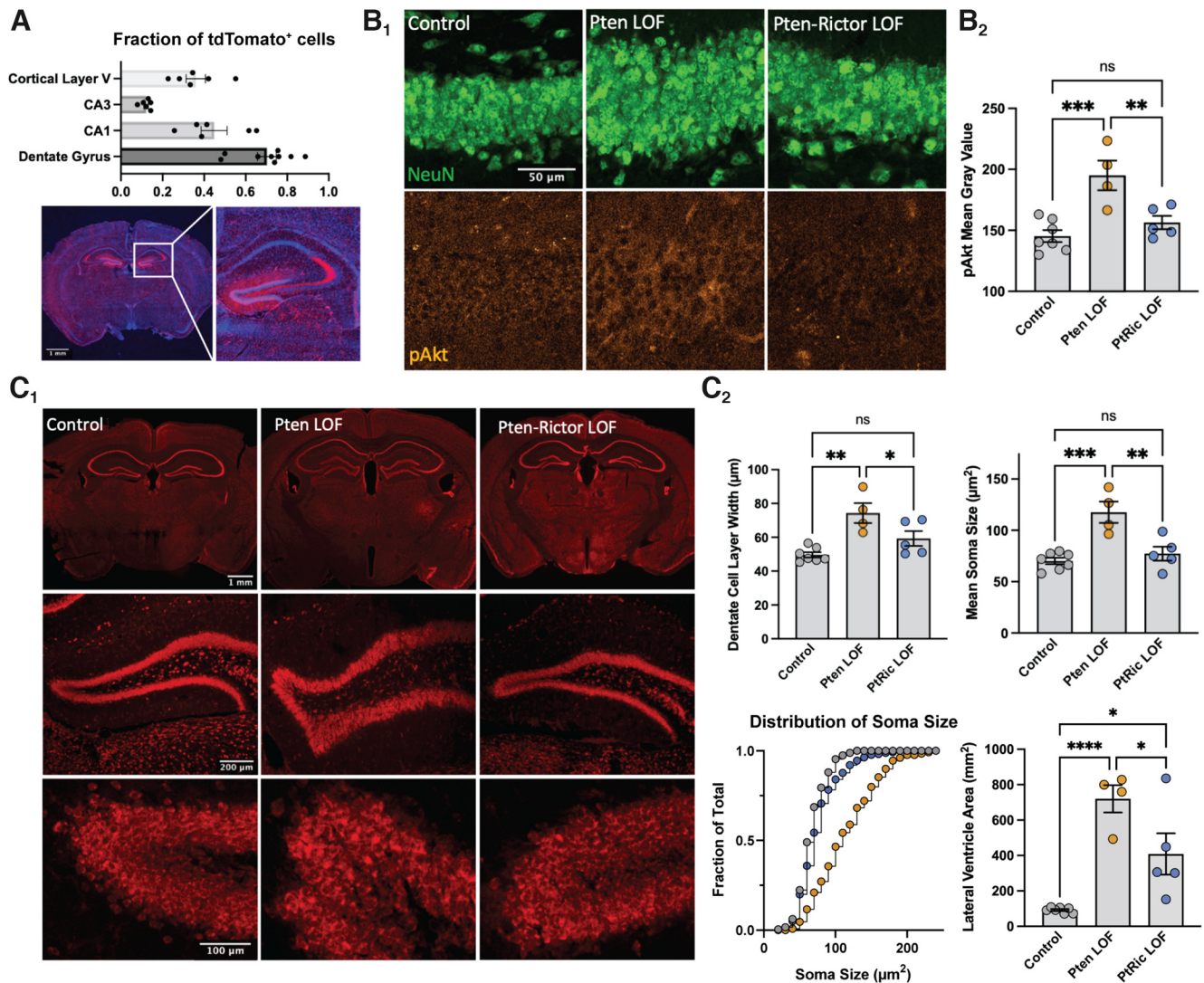


Figure 3. mTORC2 inactivation rescues increased phospho-Akt expression and dentate gyrus hypertrophy in *GFAP-Cre;Pten* LOF mice. **A**, Bar chart and representative images showing the distribution of tdTomato expression (red) in a Cre-dependent, tdTomato reporter mouse counterstained with DAPI (blue). tdTomato expression was most prominent in the dentate gyrus GCL and present to a lesser extent in CA1, CA3, and cortical layer V. Projections from the GCL can be seen medial to CA3. **B₁**, Representative images of NeuN (top row) and pAkt(473) (bottom row) immunofluorescence in the GCL of Control, Pten LOF, and Pten-Rictor-LOF mice. **B₂**, pAkt(473) signal was increased in Pten LOF neurons and decreased to Control levels in Pten-Rictor LOF ($F = 12.58$, $p = 0.0009$). **C₁**, Representative images of Neurotrace (Nissl) staining showing the impact of Pten LOF or Pten-Rictor LOF on whole brain (top row), dentate gyrus GCL (middle row), and individual DGCs (bottom row). **C₂**, Pten LOF increased, and Pten-Rictor LOF normalized, GCL width ($F = 11.09$, $p = 0.0016$) and mean DGC soma size ($F = 15.17$, $p = 0.0016$). The lateral ventricle area increase caused by Pten loss was attenuated by mTORC2 inactivation but still elevated above control levels ($F = 27.07$, $p < 0.0001$). Each dot represents the mean value of three sections from 1 mouse. Error bars indicate mean \pm SEM. ns, $p > 0.05$; * $p < 0.05$; ** $p < 0.01$; *** $p < 0.001$; **** $p < 0.0001$; one-way ANOVA with Tukey multiple comparisons correction.

seizures, mTORC2 inactivation does not protect Pten LOF animals against induced seizures.

All animals demonstrated interictal spikes, spike trains, and myoclonic jerks before the first observed generalized seizure. Visual examination of the pre-seizure EEG traces (Fig. 2C) suggested that Pten LOF and Pten-Rictor LOF animals proceeded from a quiet baseline EEG to the generalized seizure without as much pre-seizure spiking. To quantify this, we counted the number of preictal spikes in the 10 min before seizure onset (Fig. 2D). Both Pten LOF and Pten-Rictor LOF animals had fewer events immediately preceding seizures than Control animals (Fig. 2D).

Rictor LOF protects against morphologic abnormalities in outbred *Gfap-Cre;Pten* animals

In the *Gfap-Cre;Pten* model, Pten was previously reported to be deleted in the majority of DGCs, in addition to smaller populations of hippocampal and cortical pyramidal neurons, and

cerebellar granule neurons (Backman et al., 2001; Kwon et al., 2001). To confirm this, we crossed *Gfap-Cre;Pten* mice to Cre-inducible tdTomato reporter mice and observed that $\sim 70\%$ of DGCs were tdTomato⁺ (Fig. 3A). Because DGCs are sensitive to Pten loss, both *in vitro* and *in vivo*, and loss of Pten in DGCs is sufficient to cause spontaneous seizures and gross morphologic abnormalities (Kwon et al., 2006; Pun et al., 2012; Weston et al., 2012; Williams et al., 2015; LaSarge et al., 2016), we focused our mechanistic experiments on the dentate gyrus.

One of the most direct and consistent effects of Pten loss is an increase in phosphorylation of Akt at S473, which is a major target of mTORC2 (Backman et al., 2001; Kwon et al., 2001; Sarbassov et al., 2005). Thus, to assess the extent of Pten loss in the dentate gyrus of our outbred mice, we immunostained fixed sections for pAkt(S473) (Fig. 3B₁). As expected, pAkt(S473) levels were increased in the GCL in Pten LOF brains, and this increase was ameliorated by Rictor deletion (Fig. 3B₂).

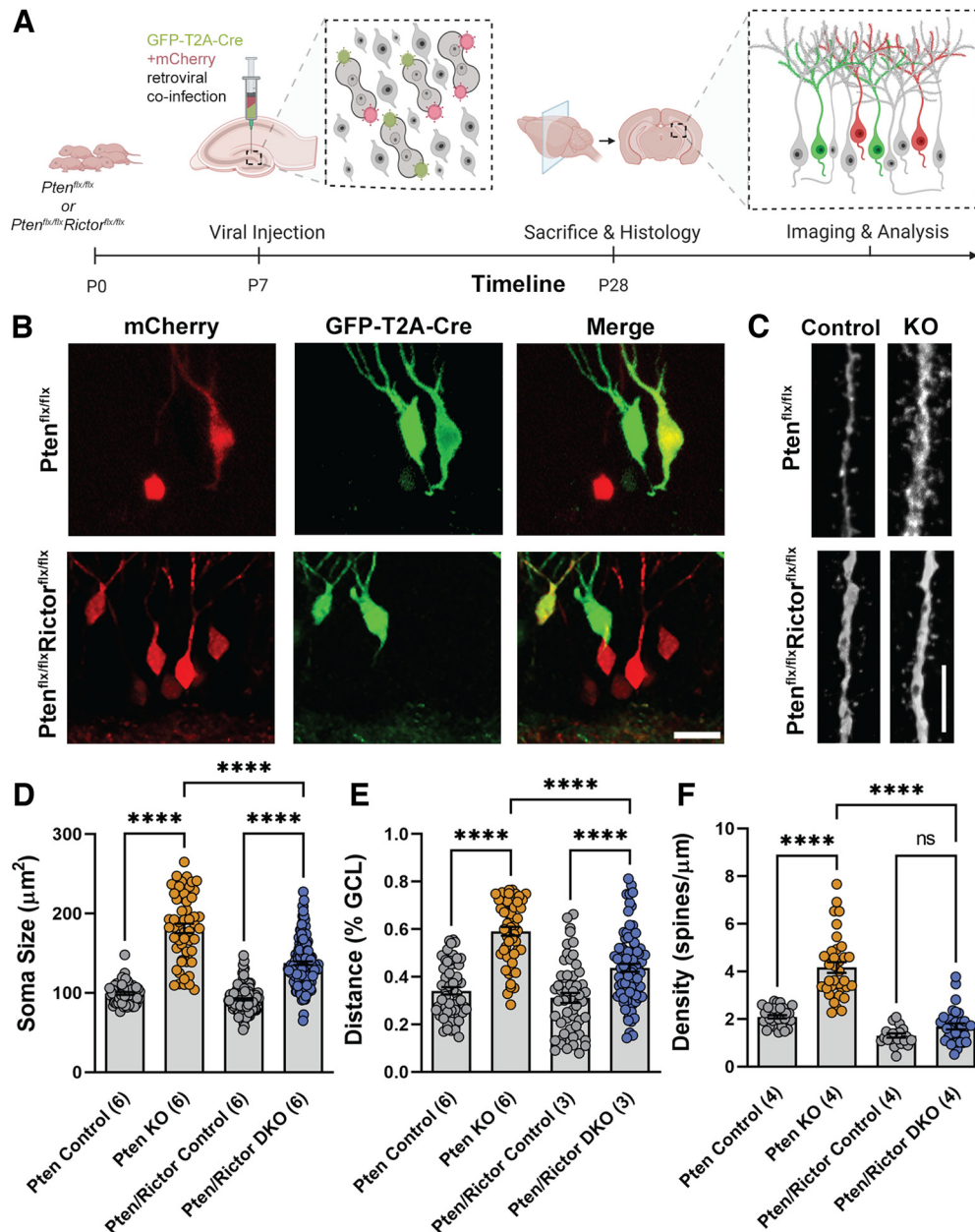


Figure 4. mTORC2 inactivation decreases *Pten* KO-mediated soma hypertrophy, aberrant migration, and increased spine density in DGCs. **A**, Schematic of the experiment. *Pten^{fl/fl}*, or *Pten^{fl/fl}/Rictor^{fl/fl}* animals were co-injected in dentate gyrus with fluorophore only (mCherry), and fluorophore and Cre recombinase (GFP-T2A-Cre) retrovirus at P7. Three weeks later, the animals were killed for histologic analyses. **B**, Top panels, Representative images of DGCs from *Pten^{fl/fl}* animals. Bottom panels, Representative images from *Pten^{fl/fl}/Rictor^{fl/fl}* animals, used for soma size and migration analysis. Scale bar, 20 μm . **C**, Representative images for spine density analysis. Scale bar, 5 μm . **D**, Pten KO-mediated soma hypertrophy was partially rescued in Pten/Rictor DKO DGCs. **** $p < 0.0001$. **E**, The farther migration of Pten KO DGCs in the GCL was partially rescued in Pten/Rictor DKO DGCs. **** $p < 0.0001$. **F**, The Pten KO-mediated increase in spine density was completely rescued in Pten/Rictor DKO DGCs. **** $p < 0.0001$. Numbers in parentheses represent the number of animals. Statistical analysis was performed using a mixed-effects model. * $p < 0.05$; ** $p < 0.01$; *** $p < 0.001$; **** $p < 0.0001$. For quantitative results, see Table 3.

PTEN LOF in DGCs (Kwon et al., 2006; Pun et al., 2012), including in the *Gfap-Cre;Pten* model, causes overgrowth of the dentate gyrus (Backman et al., 2001; Kwon et al., 2001). To evaluate gross morphologic changes in the dentate, we stained fixed sections with a fluorescent Nissl stain. In agreement with previous studies, we observed overgrowth and altered morphology of the GCL in sections from Pten LOF mice (Fig. 3C₁). The GCL width was significantly increased by Pten LOF (by almost 50%) but reduced to control levels by Pten-Rictor LOF (Fig. 3C₂). We also examined the somatic area stained by Nissl as a proxy for cell size. This was also increased by Pten LOF but reduced to control levels by Pten-Rictor LOF (Fig. 3C₂). The area of the lateral ventricles was also increased

in Pten LOF brains, which was previously observed in this model and is thought to be because of disturbances in the morphology of the cerebellum (Backman et al., 2001; Kwon et al., 2001). This increase was attenuated in Pten-Rictor LOF, but not reduced to control levels. Thus, despite a lack of protection against seizure phenotypes, mTORC2 inhibition significantly improved gross morphologic abnormalities in the dentate gyrus.

mTORC2 inactivation improves increases in cell size, migration, and dendritic overgrowth caused by PTEN loss in granule neurons
 The above data indicate that mTORC2 inactivation protects against gross morphologic changes caused by PTEN LOF. However, PTEN

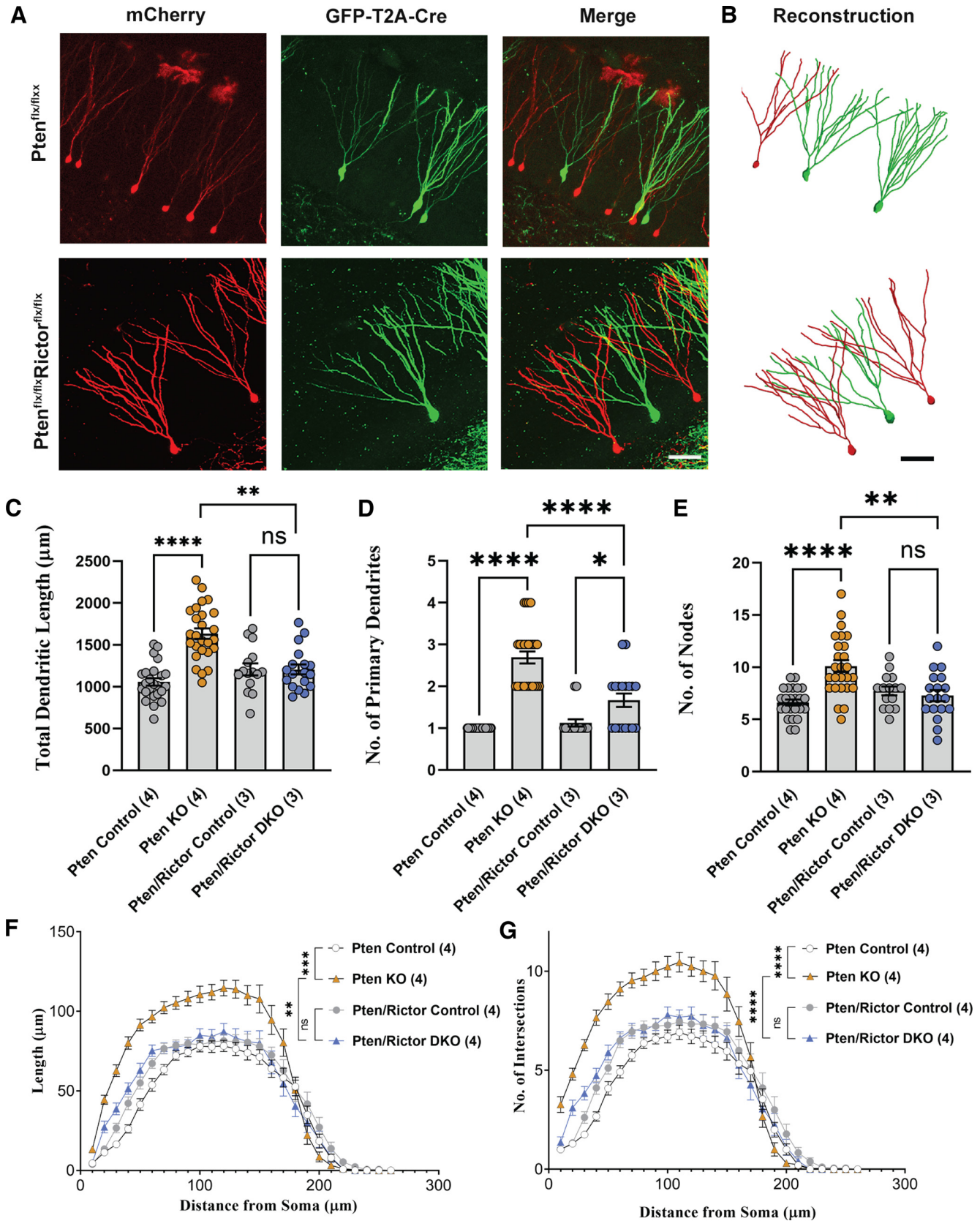


Figure 5. mTORC2 inactivation reduces *Pten* KO-mediated dendritic overgrowth in DGCs. **A**, Top panels, Representative images of fluorescent DGCs from *Pten^{flx/flx}* animals. Bottom panels, Representative images from *Pten^{flx/flx}/Rictor^{flx/flx}* animals. Scale bar, 50 μm . **B**, 3D Reconstructions of neurons in **A**. Scale bar, 50 μm . **C**, *Pten* KO-mediated increase in total dendritic length was completely rescued in *Pten/Rictor* DKO DGCS. **D**, The increase in the number of primary dendrites in *Pten* KO neurons was partially rescued in *Pten/Rictor* DKO neurons. **E**, *Pten* KO-mediated increase in dendritic nodes was completely rescued in *Pten/Rictor* DKO DGCS. **F**, *Pten/Rictor* DKO rescued the increase in Sholl length of *Pten* KO neurons. **G**, The increase in Sholl intersections of *Pten* KO neurons was rescued in *Pten/Rictor* DKO neurons. Numbers in parentheses represent the number of animals. Statistical analysis was performed using a mixed-effects model (**C–E**), or two-way ANOVA with Bonferroni’s *post hoc* (**F,G**). * $p < 0.05$. ** $p < 0.01$. *** $p < 0.001$. **** $p < 0.0001$. For complete results, see Table 3.

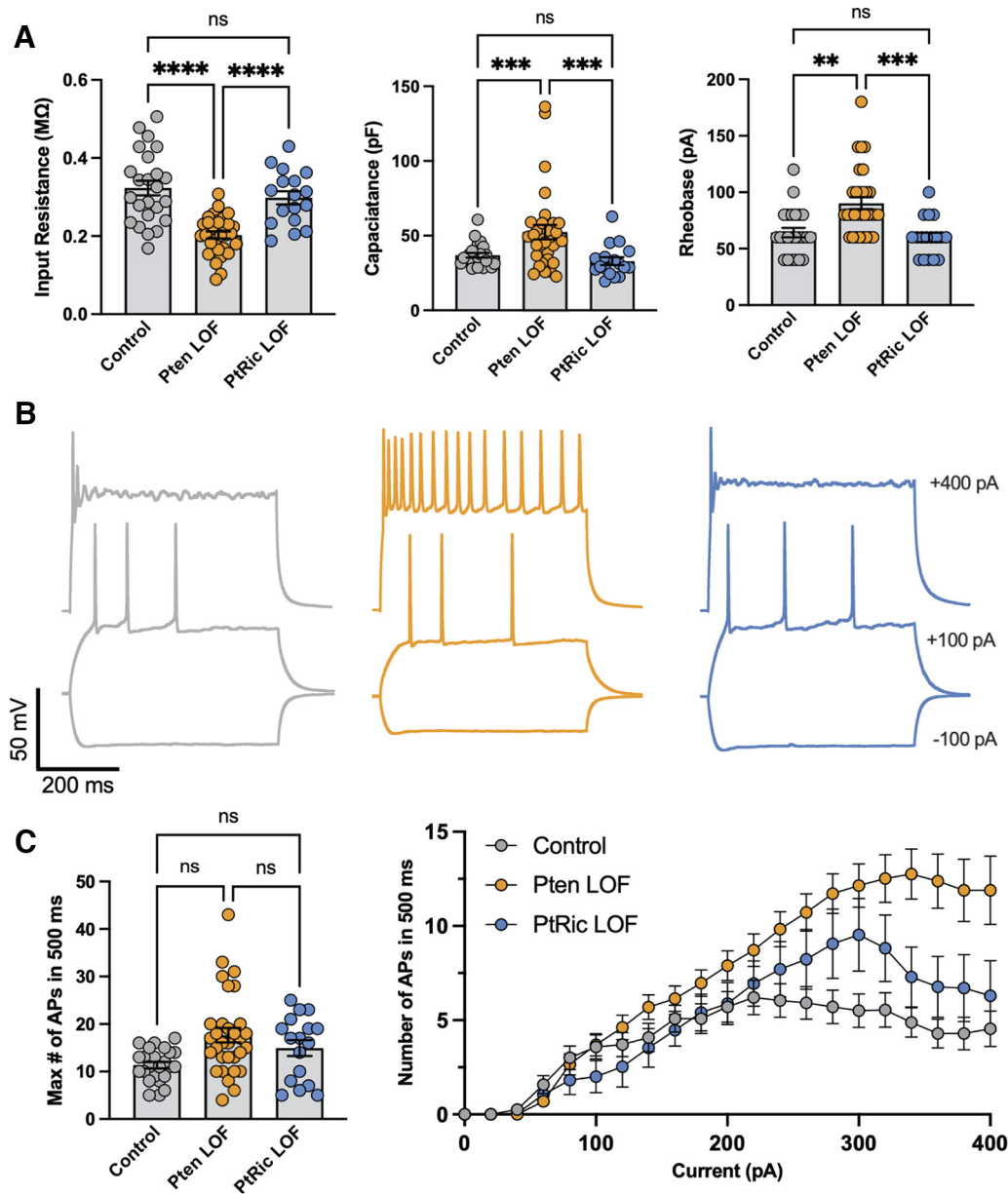


Figure 6. mTORC2 inactivation rescues membrane excitability changes in *GFAP-Cre;Pten* LOF DGCs. **A**, *Pten* LOF DGCs showed decreased input resistance, increased capacitance, and increased rheobase, all of which were reduced to Control levels in *Pten-Rictor* LOF. **B**, Representative current-clamp traces of responses to 500 ms pulses of -100 , 100 , and 400 pA current. Control and *Pten-Rictor* LOF traces show neurons that have hit depolarization block, which occurred at or before 400 pA in 17 of 24 Control neurons (70.8%), 7 of 29 *Pten* LOF neurons (24.1%), and 11 of 17 *Pten-Rictor* LOF neurons (64.7%). **C**, Maximum AP firing rate was increased in *Pten* LOF and partially attenuated in *Pten-Rictor* LOF. Although the increase in maximum firing rate was not significant (left graph), *Pten* LOF neurons fired significantly more APs than Control neurons at all current levels >280 pA, partially rescued by *Pten-Rictor* LOF (Current \times genotype interaction, $p = 0.05$). Each dot represents the value of one neuron, except for the AP/I plot, where dots are means. Error bars indicate mean \pm SEM. ns, $p > 0.05$; * $p < 0.05$; ** $p < 0.01$; *** $p < 0.001$; **** $p < 0.0001$; tested with GEEs.

LOF causes several other changes in neuronal morphology, such as increased dendrite growth and spine density, that may also contribute to epilepsy and other circuit abnormalities (LaSarge and Danzer, 2014; LaSarge et al., 2021). To examine these cellular and subcellular effects in more detail, we expressed Cre in a small percentage of DGCs, allowing us to resolve the morphology of individual neurons.

To do this, we coinjected two retroviruses into the dentate gyrus of *Pten^{fl/fl};Rictor^{+/+}* and *Pten^{fl/fl};Rictor^{fl/fl}* mice at P7 and compared their neuronal morphology revealed by the cell-filling fluorophores. One virus expressed GFP with a downstream Cre, and the other expressed mCherry with no Cre. Thus, the GFP-expressing newborn DGCs are KO for their respective floxed genes, while

mCherry-expressing DGCs serve as their in-tissue WT controls (Fig. 4A). Immunohistochemical analysis at P28 revealed that *Pten* KO DGCs had greater soma size when compared with their WT control; and similar to the results from the Nissl analysis (Fig. 3C₂), this increase in soma size was reduced in *Pten/Rictor* DKO neurons (Fig. 4B,D), although in this analysis the *Pten/Rictor* DKO neurons were still significantly larger than control neurons. *Pten* KO neurons also migrated farther from the hilus along the GCL, compared with their WT control, and this migration defect was also partially rescued in *Pten/Rictor* DKO neurons (Fig. 4E). There was also an increase in the number of dendritic spines on *Pten* KO neurons in the middle molecular layer, which was completely rescued in *Pten/Rictor* DKO neurons (Fig. 4C,F).

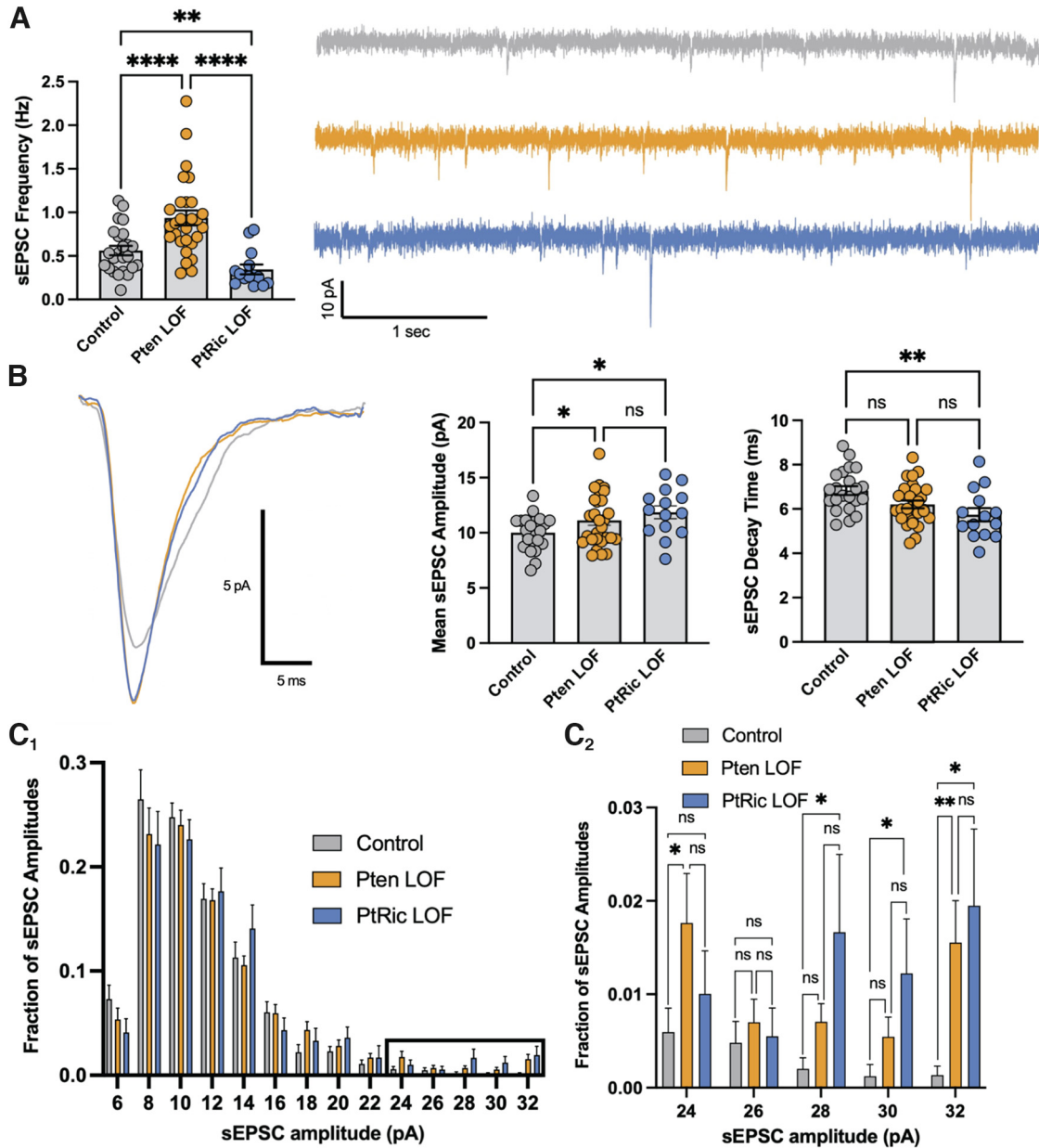


Figure 7. mTORC2 inactivation reduces frequency but increases the strength of spontaneous excitatory currents in *GFAP-Cre;Pten* LOF DGCs. **A**, Summary data and example traces showing sEPSC frequency in DGCs is increased in Pten LOF and rescued to Control levels in Pten-Rictor LOF. **B**, Example traces and summary data showing that sEPSC amplitude was increased from Control by Pten-Rictor LOF and Pten LOF. The mean decay time of sEPSCs was decreased from Control in Pten-Rictor LOF, but not Pten LOF. **C₁**, Relative frequency histogram showing the distribution of sEPSC amplitudes. **C₂**, Blowup of the highest amplitude bins from the frequency histogram shows that high-amplitude sEPSCs make up a significantly greater fraction of the total in Pten LOF and Pten-Rictor LOF DGCs. Each dot represents the value of one neuron. Error bars indicate mean \pm SEM. ns, $p > 0.05$; * $p < 0.05$; ** $p < 0.01$; *** $p < 0.001$; **** $p < 0.0001$; tested with GEEs (**A,B**) or GLM (**C₂**).

Because alterations in dendritic growth and patterning are hallmarks of PTEN LOF, we next reconstructed dendrites of Pten KO and Pten/Rictor DKO in 3D (Fig. 5A,B). Total dendritic length was increased in Pten KO neurons, and the Pten/Rictor DKO fully rescued this increase (Fig. 5C). An increase in the number of primary dendrites sprouting directly out of the soma, as previously observed in Pten KO DGCs (Skelton et al., 2020), was partially rescued by Pten/Rictor DKO (Fig. 5D). The dendritic arbor of Pten KO neurons also had an increased number of branch points (nodes) compared with WT, and this increase was rescued in Pten/Rictor DKO neurons (Fig. 5E). Sholl of length analysis revealed that, as the distance from the soma increased,

Pten KO neurons had acquired a greater dendritic length at each 10 μ m interval, compared with their WT control, and Pten/Rictor DKO rescued this increase (Fig. 5F). Similarly, Sholl of intersections analysis revealed that, as the distance from the soma increased, Pten KO neurons had a greater number of dendritic branches intersecting the 10 μ m intervals compared with their WT control, and Pten/Rictor DKO also rescued this increase (Fig. 5G). Thus, *Rictor* loss was able to completely rescue features of neuronal hypertrophy distal to the soma, such as dendritic length, branching, and spine density, and partially rescued features proximal to the soma, such as soma size and the number of primary dendrites (Table 2).

Table 2. Morphologic data from retrovirally infected granule neurons

Genotype	Cre	Soma size (mean \pm SEM; μm^2)	<i>p</i>	<i>n</i> , cells (animals)
<i>Pten</i> ^{flx/flx}	–	102.40 \pm 2.94	<0.0001	57 (6)
<i>Pten</i> ^{flx/flx}	+	181.24 \pm 5.80		55 (6)
<i>Pten</i> ^{flx/flx} <i>Rictor</i> ^{flx/flx}	–	91.85 \pm 1.28	<0.0001	141 (6)
<i>Pten</i> ^{flx/flx} <i>Rictor</i> ^{flx/flx}	+	136.55 \pm 1.83		240 (6)
<i>Pten</i> ^{flx/flx}	+	181.24 \pm 5.80	<0.0001	55 (6)
<i>Pten</i> ^{flx/flx} <i>Rictor</i> ^{flx/flx}	+	136.55 \pm 1.83		240 (6)
Migration (mean \pm SEM; % GCL)				
<i>Pten</i> ^{flx/flx}	–	0.340 \pm 0.01	<0.0001	57 (6)
<i>Pten</i> ^{flx/flx}	+	0.583 \pm 0.01		55 (6)
<i>Pten</i> ^{flx/flx} <i>Rictor</i> ^{flx/flx}	–	0.311 \pm 0.02	<0.0001	54 (6)
<i>Pten</i> ^{flx/flx} <i>Rictor</i> ^{flx/flx}	+	0.409 \pm 0.01		142 (6)
<i>Pten</i> ^{flx/flx}	+	0.583 \pm 0.01	<0.0001	55 (6)
<i>Pten</i> ^{flx/flx} <i>Rictor</i> ^{flx/flx}	+	0.409 \pm 0.01		142 (6)
Spine density (mean \pm SEM; #)				
<i>Pten</i> ^{flx/flx}	–	2.09 \pm 0.06	<0.0001	32 (4)
<i>Pten</i> ^{flx/flx}	+	4.54 \pm 0.30		38 (4)
<i>Pten</i> ^{flx/flx} <i>Rictor</i> ^{flx/flx}	–	1.30 \pm 0.08	<0.0001	22 (4)
<i>Pten</i> ^{flx/flx} <i>Rictor</i> ^{flx/flx}	+	1.68 \pm 0.12		34 (4)
<i>Pten</i> ^{flx/flx}	+	4.54 \pm 0.30	0.370	38 (4)
<i>Pten</i> ^{flx/flx} <i>Rictor</i> ^{flx/flx}	+	1.68 \pm 0.12		34 (4)
Dendritic length (mean \pm SEM; μm)				
<i>Pten</i> ^{flx/flx}	–	1056.29 \pm 45.08	<0.0001	24 (4)
<i>Pten</i> ^{flx/flx}	+	1634.42 \pm 62.69		26 (4)
<i>Pten</i> ^{flx/flx} <i>Rictor</i> ^{flx/flx}	–	1206.77 \pm 71.37	<0.01	15 (3)
<i>Pten</i> ^{flx/flx} <i>Rictor</i> ^{flx/flx}	+	1206.17 \pm 58.62		18 (3)
<i>Pten</i> ^{flx/flx}	+	1634.42 \pm 62.69	1.000	26 (4)
<i>Pten</i> ^{flx/flx} <i>Rictor</i> ^{flx/flx}	+	1206.17 \pm 58.62		18 (3)
Primary dendrites (mean \pm SEM; #)				
<i>Pten</i> ^{flx/flx}	–	1 \pm 0	<0.0001	24 (4)
<i>Pten</i> ^{flx/flx}	+	2.69 \pm 0.14		26 (4)
<i>Pten</i> ^{flx/flx} <i>Rictor</i> ^{flx/flx}	–	1.125 \pm 0.08	<0.05	16 (3)
<i>Pten</i> ^{flx/flx} <i>Rictor</i> ^{flx/flx}	+	1.66 \pm 0.16		18 (3)
<i>Pten</i> ^{flx/flx}	+	2.69 \pm 0.14	<0.0001	26 (4)
<i>Pten</i> ^{flx/flx} <i>Rictor</i> ^{flx/flx}	+	1.66 \pm 0.16		18 (3)

mTORC2 inactivation rescues changes in membrane properties of granule neurons

Because *Rictor* loss largely protected against morphologic changes, but not epileptic activity, caused by PTEN LOF, we hypothesized that it may not rescue all the functional effects of PTEN LOF. To test which functional effects of PTEN loss are rescued by mTORC2 inhibition, we performed whole-cell, current-clamp recordings of Control, *Pten* LOF, and *Pten*-*Rictor* LOF DGCs from acute hippocampal slices (6 litters; 1 or 2 animals per litter; 2–4 slices per animal; 1–5 neurons per slice, Fig. 6). Previous studies showed that PTEN loss in DGCs reduces input resistance, increases membrane capacitance, and increases the rheobase current, changes that are likely linked to increased somatic and dendritic growth (Weston et al., 2012; Williams et al., 2015; Santos et al., 2017). Consistent with these data, we found that input resistance was significantly decreased, whereas rheobase and capacitance were increased by *Pten* LOF (Fig. 6A,B). All of these alterations were rescued to control levels by *Rictor* LOF (Fig. 6A,B), which agrees with the rescue of cellular and dendritic morphology (Figs. 3–5). There were no differences between any of the groups in single AP properties (threshold, half-width, amplitude, or amplitude of afterhyperpolarization, Table 3). Analysis of AP frequency versus current plots, however, showed a significant increase in AP firing caused by *Pten* LOF at all levels >280 pA. *Pten*-*Rictor* LOF neurons had AP frequencies that were significantly higher than Control (280–320 pA), but still significantly less than *Pten* LOF (320 pA), indicating a partial rescue

(Fig. 6C). Thus, similar to morphologic alterations, the membrane and AP firing impairments caused by PTEN LOF were largely rescued by mTORC2 inactivation.

mTORC2 inactivation rescues the frequency of excitatory synaptic events onto DGCs but not their strength

To determine whether synaptic activity onto DGCs differs between Control, *Pten* LOF, and *Pten*-*Rictor* LOF neurons, we performed whole-cell, voltage-clamp recordings of sEPSCs in acute slices. Similar to previous findings, the frequency of sEPSCs received by *Pten* LOF neurons was increased, and this increase was rescued to even below control levels by *Pten*-*Rictor* LOF (Fig. 7A; Table 3), which is consistent with the increase and rescue of dendritic spine density (Fig. 4F). We also examined the mean amplitude and decay time of the sEPSCs, as previous studies have found increases in EPSC amplitudes caused by *Pten* LOF onto DGCs (Luikart et al., 2011b; Williams et al., 2015). sEPSC amplitude was increased by *Pten* LOF, an effect that was not rescued in *Pten*-*Rictor* LOF neurons (Fig. 7B). We also found that the decay time of sEPSCs was faster onto *Pten*-*Rictor* LOF neurons than Control (Fig. 7B).

To better understand why the mean sEPSC amplitude was increased by *Pten* and *Pten*-*Rictor* LOF, we investigated the amplitude distribution of sEPSCs by plotting the amplitudes on a relative frequency histogram (Fig. 7C₁). Although the overall shapes of these histograms were similar between genotypes, investigation of the largest amplitude bins showed that a class of high-amplitude sEPSCs was present to a significantly greater degree in *Pten* LOF and *Pten*-*Rictor* LOF compared with Control neurons (Fig. 7C₂). There were no significant differences between *Pten* LOF and *Pten*-*Rictor* LOF in the high-amplitude bins. These results indicate that, although mTORC2 inactivation can normalize the increase in the total number of synaptic inputs that *Pten* LOF DGCs receive, it cannot normalize a class of abnormally strong and fast synapses.

mTORC2 inhibition rescues aberrant synapse formation in the dentate gyrus IML, but not in the GCL

Synaptic events onto the somas and proximal dendrites of neurons generally appear larger and decay faster than those made onto distal dendrites when recorded at the soma, because of the impact of dendritic filtering and imperfect voltage clamp. Thus, we hypothesized that the increase in amplitude and the decrease in decay time of sEPSCs onto *Pten*-*Rictor* LOF neurons are caused by an increase in the fraction of synapses close to their somas. To test this, we stained coronal slices for VGLUT1 to assess glutamatergic innervation of the dentate GCL, which largely contains DGC somas, and IML, which largely contains DGC dendrites (Fig. 8A). VGLUT1 expression was increased in the IML and GCL in the *Pten* LOF dentate gyrus. However, in *Pten*-*Rictor* LOF dentate gyrus, VGLUT1 expression was only increased within the GCL (Fig. 8B). This constrained increase in synapse formation could account for the class of high-amplitude, fast-decay sEPSC events observed onto *Pten*-*Rictor* LOF neurons. Additionally, the influence of this selective increase in proximal excitatory connectivity could predispose *Pten*-*Rictor* LOF brains to seizure despite the rescue of more distal aberrant connectivity.

mTORC2 inactivation does not rescue cell-autonomous increases in synaptic transmission induced by PTEN LOF

The above results suggest that mTORC2 inactivation via *Rictor* loss may not be sufficient to prevent increases in synaptic

Table 3. Electrophysiological properties of DGs recorded in slice preparation^a

Property	Control (EMM ± SEM)	Pten LOF (EMM ± SEM)	Pten-Rictor LOF (EMM ± SEM)	GEE <i>p</i> values		
				Con-PTEN	Con-PtRi	PTEN-PtRi
Input resistance (MΩ)	323 ± 19	202 ± 11	300 ± 22	<0.0001	0.44	<0.0001
Capacitance (pF)	37.1 ± 2.2	49.9 ± 2.6	32.8 ± 2.4	0.0003	0.19	0.0001
Rheobase (pA)	63.1 ± 4.7	90.7 ± 6.2	59.9 ± 5.3	0.001	0.65	0.0004
AP threshold (mV)	−30.0 ± 1.1	−33.1 ± 0.91	−29.7 ± 1.3	0.08	0.83	0.08
AP amplitude (mV)	64.2 ± 2.2	70.5 ± 2.1	66.9 ± 2.84	0.11	0.60	0.60
AP half-width (ms)	2.12 ± 0.12	1.79 ± 0.12	1.93 ± 0.13	0.13	0.50	0.50
AHP amplitude (mV)	7.06 ± 0.82	7.84 ± 0.70	8.89 ± 1.01	0.64	0.41	0.64
Max AP rate (Hz)	22.6 ± 3.0	35.8 ± 4.8	28.4 ± 4.4	0.057	0.43	0.43
sEPSC frequency (Hz)	0.53 ± 0.05	0.96 ± 0.09	0.39 ± 0.04	<0.0001	0.004	<0.0001
sEPSC amplitude (pA)	9.8 ± 0.34	11.1 ± 0.36	11.7 ± 0.56	0.027	0.017	0.37

^aEMM, Estimated marginal means. All statistics were calculated with GEEs in SPSS with genotype as a factor and age as a covariate.

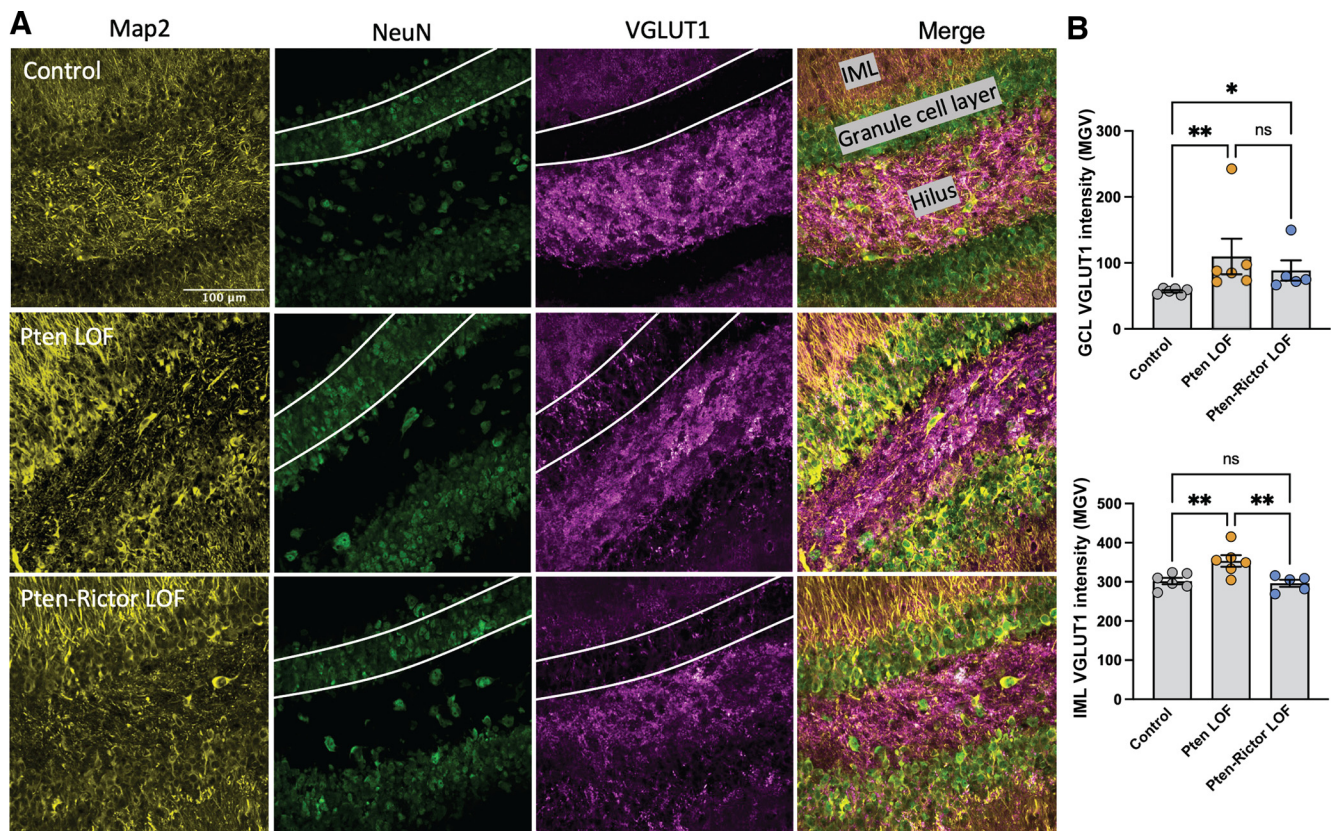


Figure 8. mTORC2 inactivation rescues excitatory hyperconnectivity in the dentate gyrus IML, but not the GCL. **A**, Representative images of MAP2 (left), NeuN (middle left), and VGLUT1 (middle right) fluorescence in the dentate gyrus GCL, IML, and hilus. **B**, VGLUT1 fluorescence was increased in Pten LOF brains in the GCL and IML. The increase in the IML ($F = 7.778$, $p = 0.0053$) was rescued by mTORC2 inactivation, but the increase in the GCL (Kruskal–Wallis test; $K = 11.7$, $p = 0.0002$) was not. Each dot represents the mean value of three sections from 1 mouse. Error bars indicate mean ± SEM. ns, $p > 0.05$; * $p < 0.05$; ** $p < 0.01$; Kruskal–Wallis test with Dunn’s multiple comparisons test (GCL) or one-way ANOVA with Tukey multiple comparisons correction (IML).

transmission caused by PTEN LOF. However, the presence of seizures in Pten-Rictor LOF animals could drive these changes in synaptic transmission. Previously, using a single-neuron culture system, we showed that PTEN LOF induces cell-autonomous increases in synaptic transmission that can be prevented by rapamycin treatment (Weston et al., 2012). To test whether mTORC2 inhibition alone is sufficient to prevent these increases, we created single-neuron cultures of Control, Pten LOF, and Pten-Rictor LOF hippocampal neurons and quantified several parameters of presynaptic and postsynaptic glutamatergic transmission in the absence of the confound of seizure or activity-dependent alterations.

As expected, Pten LOF caused an increase in the peak amplitude of eEPSCs (Fig. 9A). Pten-Rictor LOF did not rescue this

increase, as the amplitude of eEPSCs from Pten-Rictor LOF neurons was significantly larger than eEPSC from Control neurons and not different from Pten LOF neurons (Fig. 9A). This lack of rescue occurred, although pAKT(473) levels were significantly increased in Pten LOF neurons and reduced to less than control levels in Pten-Rictor LOF neurons (Fig. 9B), and several intrinsic properties were largely normalized (Table 4).

Previously, we showed that the increase in eEPSC amplitude following PTEN loss is because of increases in the amplitude of the postsynaptic response to single SV fusion (quantal size) and the number of fusion-competent SVs (readily releasable pool [RRP]). Because Pten-Rictor LOF did not rescue the eEPSC amplitude, we predicted it would also not rescue these underlying

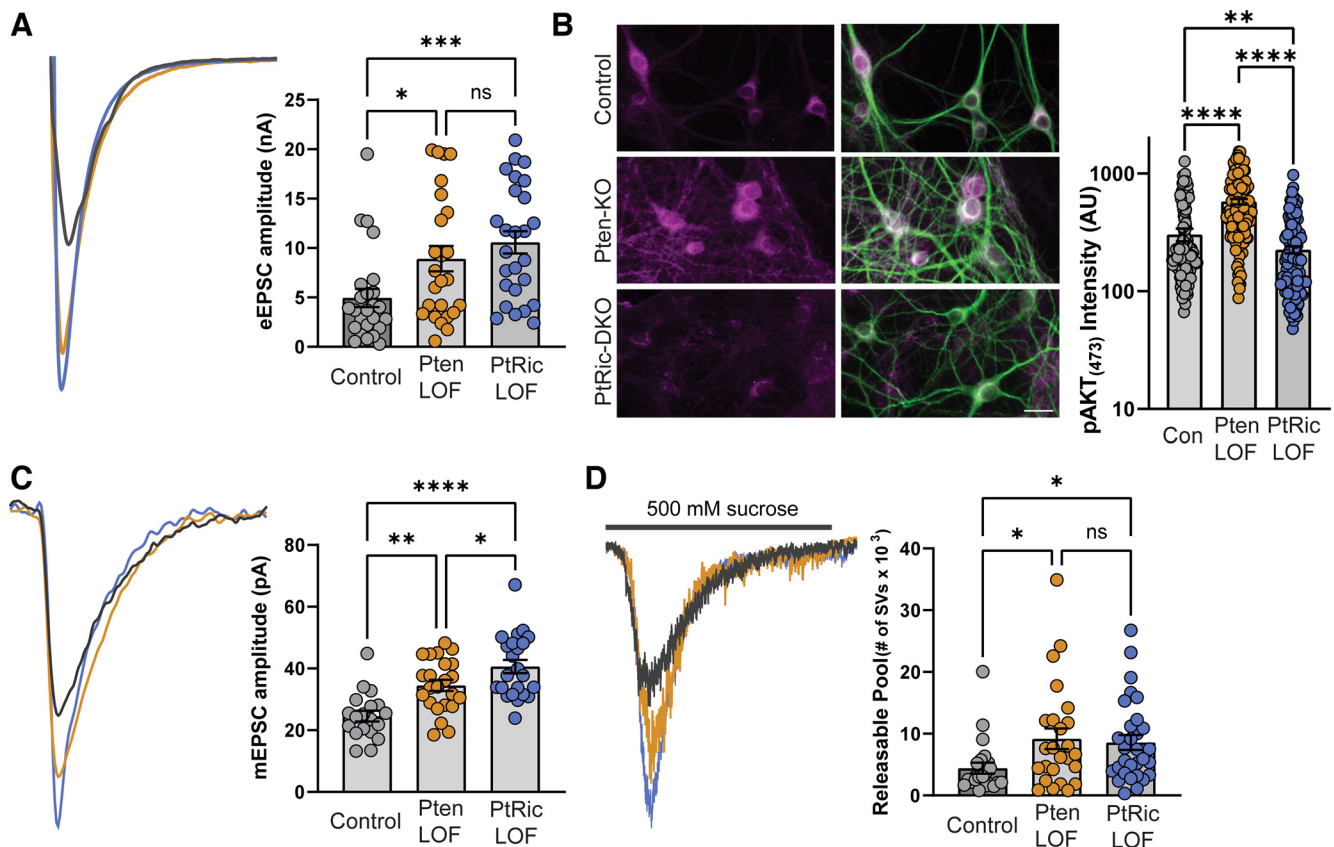


Figure 9. mTORC2 inactivation does not prevent cell-autonomous increases in excitatory synaptic transmission in cultured single neurons. **A**, Example traces and dot plot showing the peak amplitude of evoked EPSCs is increased by Pten LOF and not rescued by mTORC2 inactivation. **B**, Representative images of immunofluorescence using antibodies against pAkt (magenta, left panels), and pAkt overlaid with MAP2 (green, right panels). Scale bar, 25 μ m. Summary dot plot showing the increase in pAkt staining caused by Pten LOF and the reduction below Control levels in Pten-Rictor LOF neurons. **C**, Example traces and dot plot showing the peak amplitude of mEPSCs is increased by Pten LOF and not rescued by mTORC2 inactivation. **D**, Example traces (left) showing the current response to 4 s application of 500 mM sucrose. Right, Summary dot plot showing the number of SVs in the RRP of neurons from each genotype. Error bars indicate mean \pm SEM. * $p < 0.05$; ** $p < 0.01$; *** $p < 0.001$; **** $p < 0.0001$; tested with GEEs.

Table 4. Intrinsic electrophysiological properties of cultured neurons

Property	Control (mean \pm SEM)	Pten LOF (mean \pm SEM)	Pten-Rictor LOF (mean \pm SEM)	GEE p
Input resistance ($m\Omega$)	301.8 \pm 23.6	190.1 \pm 16.5	268.8 \pm 23.9	0.0021
Capacitance (pF)	81.1 \pm 5.3	123.7 \pm 9.9	105.8 \pm 7.6	0.0011
Rheobase (pA)	124.3 \pm 24.2	244.7 \pm 30.1	106.7 \pm 13.5	0.0003
AP threshold (mV)	-36.1 \pm 1.87	-35.6 \pm 1.9	-40.7 \pm 2.96	0.038
AP amplitude (mV)	70.4 \pm 2.8	73.3 \pm 3.3	77.0 \pm 3.6	0.512
AP half-width (ms)	2.08 \pm 0.22	2.03 \pm 0.19	1.95 \pm 0.15	0.248

parameters. To test how Pten-Rictor LOF affects quantal size, we recorded mEPSCs and measured their amplitude. Pten LOF increased the peak amplitude of mEPSCs; and similar to the results from slice recordings (Fig. 7B), the amplitude of Pten-Rictor LOF mEPSCs was increased above the Control level (Fig. 9C). The number of release-ready SVs was also increased by Pten LOF and not rescued by Pten-Rictor LOF (Fig. 9D). Overall, these data suggest that, despite its ability to normalize AKT phosphorylation, Rictor LOF does not block or rescue cell-autonomous increases in excitatory synaptic transmission caused by PTEN LOF.

mTORC2 inactivation causes further disruption to presynaptic function

Previously, we showed that *Rictor* loss alone causes impairments of presynaptic function, including lowered release probability

and increased short-term plasticity (McCabe et al., 2020), so we next tested whether Pten-Rictor LOF neurons also show these alterations. We measured the vesicular release probability by calculating the fraction of the RRP that was released by an AP. Although Pten LOF neurons were not significantly different from Control neurons, Pten-Rictor LOF neurons had a lower release probability than both Control and Pten LOF groups (Fig. 10A). This decrease was corroborated by an increase in the paired pulse ratios at interstimulus intervals of 20, 50, 100, and 200 ms (Fig. 10B,C). To assess short-term plasticity, we stimulated neurons at 10 Hz (Fig. 10D). Consistent with previous findings, Pten LOF neurons showed less depression than Control neurons (Fig. 10E); furthermore, Pten-Rictor LOF neurons showed even less depression during a 10 Hz train than Control and Pten LOF neurons (Fig. 10E). Thus, in addition to not rescuing increases in synaptic strength caused by Pten LOF (Fig. 9),

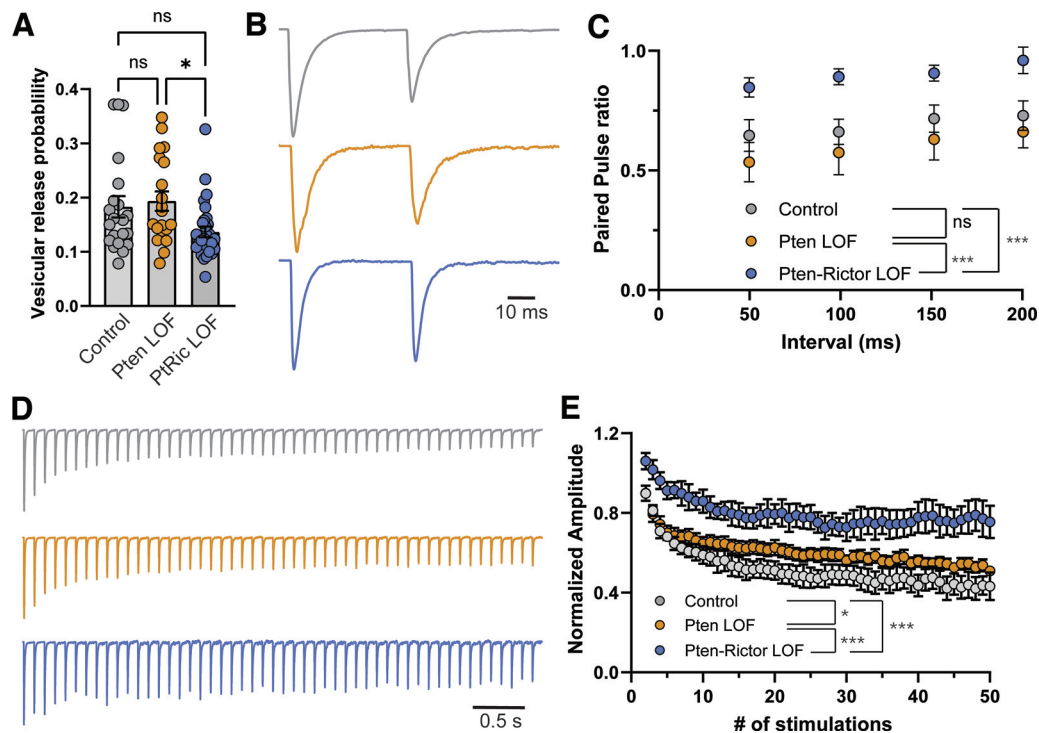


Figure 10. mTORC2 inactivation causes further impairments in presynaptic transmission, including increased short-term plasticity. **A**, Dot plot showing that the vesicular release probability, calculated as the fraction of the total RRP released per AP, is unchanged by Pten LOF but decreased by Pten-Rictor LOF. **B**, Example traces of paired EPSCs evoked with a 50 ms interstimulus interval for each genotype. **C**, Summary of the paired pulse ratio at four different interstimulus intervals showing an increase over Control and Pten-LOF in Pten-Rictor LOF neurons. **D**, Example traces of the current response to 50 stimulations at 100 ms interval for each genotype. **E**, Summary data showing less short-term depression in Pten LOF and Pten-Rictor LOF neurons compared with Control. Error bars indicate mean \pm SEM. * $p < 0.05$; ** $p < 0.01$; *** $p < 0.001$; tested with GEEs.

mTORC2 inactivation further exacerbates impairments in presynaptic function.

Discussion

The prevailing view of mTORopathies has been that mTORC1 hyperactivation mediates most of the cellular, network, and *in vivo* phenotypes seen across multiple mTORopathy models, such as increased cell growth, hyperexcitability, seizures, and behavioral abnormalities (Crino, 2016; Moloney et al., 2021). In support of this view, many mTORopathy gene variants, including those in *TSC1/2*, *DEPDC5*, and *RHEB*, are closely upstream of mTORC1 and do not activate mTORC2. Also, rapamycin and its analogs, which are thought to be relatively specific for mTORC1, showed success in treating these phenotypes. However, not all mTORopathies are equivalent. As human genetic studies have expanded the list of variants in genes that both regulate mTOR signaling and cause neurologic disease, so has our understanding that both the clinical presentations and molecular mechanisms underlying them are highly heterogeneous.

An example of this heterogeneity is the recent finding that both epilepsy and behavioral phenotypes in a mouse model of PTEN LOF, in which both mTORC1 and mTORC2 are hyperactivated, can be blocked by mTORC2, but not mTORC1 inhibition (Chen et al., 2019). We set out to further test this hypothesis in an additional PTEN LOF model for two reasons: (1) to expand the rigor of this finding by testing other cell types and circuits; and (2) to further delineate the mechanisms that mediate epileptogenesis downstream of PTEN LOF. We found that mTORC2 inhibition was not able to block seizures caused by PTEN loss under control of the *Gfap* promoter, which drives Cre expression in the majority of granule neurons in the dentate gyrus, as well as

other hippocampal, cortical, and cerebellar granule neurons (Fig. 3A). Although mTORC2 inhibition was sufficient to ameliorate several PTEN LOF-induced phenotypes in the dentate gyrus, especially morphologic ones, it did not normalize synaptic transmission and connectivity, and even caused *de novo* changes, such as increased short-term plasticity. The alterations in synaptic connectivity were also present in both fixed brain tissue and in single cultured neurons, suggesting that it does not depend on the lack of rescue of epileptiform activity. Together, these results implicate synaptic dysfunction, in the absence of characteristic morphologic changes, in epilepsy induced by PTEN LOF.

The impact of mTORC2 inactivation on outcomes downstream of PTEN LOF

Previous studies have shown that *Pten* deletion driven by several different promoters [*Gfap* (Backman et al., 2001; Ljungberg et al., 2009), *CaMKIIa* (McMahon et al., 2012; Chen et al., 2019), *POMC* (Matsushita et al., 2016), and *Gli1* (Pun et al., 2012)] can lead to epilepsy, but it is unknown whether they are all through shared mechanisms. The findings that mTORC2 inactivation can prevent epilepsy in the *CaMKIIa* model, but not ours, suggest that distinct mechanisms may underlie seizures in the two models. There are several differences between the two model systems that could underlie these divergent outcomes. First, the *CamKIIa* promoter used by Chen et al. (2019) is active in a set of neurons (glutamatergic neurons throughout the forebrain and hippocampus) that only partially overlaps with our *Gfap* model (Fig. 1A). Although our model has dense loss of PTEN in DGCs, the amount of Cre expression in the DG varies considerably between different *CamKIIa*-Cre lines (Tsien et al., 1996; Dragatsis and Zeitlin, 2000). This raises the possibility that DGCs are unique in

their unresponsiveness to mTORC2 inhibition. Interestingly, we observed that *Rictor* deletion alongside *Pten* KO completely rescues changes in dendritic arborization distal to the soma (branching and total arborization), while only partially rescuing features of *Pten* deletion proximal to the soma (soma size, increased number of primary dendrites, and increased glutamatergic input). This is congruent with the increased VGLUT1 staining in the GCL and increased EPSC amplitudes. Because *Rictor* appears more necessary for changes in distal arbors, there may be a differential degree of rescue in cells of varying morphology. Dentate granule neurons are relatively compact, while hippocampal and cortical pyramidal neurons have larger distal arbors. Our *Gfap* promoter affects relatively few of these neurons. Thus, it is possible that the protection provided by mTORC2 inactivation, while sufficient to block epileptogenesis in cortical circuits, is insufficient to protect the dentate gyrus from the same molecular insult.

Second, the onset of expression of Cre under the control of this *CaMKIIa* promoter likely occurs later than Cre expression under control of the *Gfap* promoter used in the present study. *Gfap*-Cre is expressed in the majority of DGCs by P5 (Kwon et al., 2001). Although Cre expression in a *CaMKIIa* transgenic line has been detected as early as P3 (Casanova et al., 2001), its expression continues to develop through at least the third postnatal week (Tsien et al., 1996). Thus, seizures observed in the *CaMKIIa* model could be generated by brain regions and neural circuits that were not tested in the current model. In contrast, seizures observed in our model could be occurring because of developmental vulnerabilities that occur too early to be impacted by the *CaMKIIa* model. Developmental timing is one of many important considerations in modeling mTOR dysfunction (Nguyen and Bordey, 2021).

Finally, the genetic background of the mice could also contribute to the differences in outcomes. It is known that genetic background can have strong effects on the expression of PTEN LOF phenotypes. In this study, we found that outcrossing the original *Gfap-Cre;Pten^{fl/fl}* line to the Raptor and Rictor mice on a C57BL/6J background had a strong effect on several phenotypes (Fig. 1). Also, *Pten* deletion using *Nkx2.1-Cre* in a pure C57BL/6J background is lethal within the first month of life, but in a CD-1 background mice live to adulthood (Vogt et al., 2015; Vogt, Rubenstein, Luikart, unpublished observation). The *CaMKIIa-Cre* *Pten*-Rictor LOF mice were on a pure C57B/6J background, while the mice used in the present study were on a mixed background.

Despite these differences, the present study corroborates several observations reported in Chen et al. (2019). *Pten*-Raptor LOF animals in that study displayed seizures, but not macrocephaly, which agrees with our finding that gross morphologic and epileptogenic changes induced by PTEN LOF are segregable. These convergent results align with previous observations that migration deficits induced by mTORC1 hyperactivity are neither necessary nor sufficient to generate seizures (Hsieh et al., 2016; Proietti Onori et al., 2021). This emerging theme in the literature provides reason to search for epileptogenic mechanisms downstream of mTOR dysfunction, even in the absence of gross morphologic abnormalities. Additionally, both studies found similar *Pten* deletion-induced disturbances in neuronal firing rate and sEPSC frequency, and similar rescue by *Rictor* deletion, despite recording in separate regions of the hippocampus. However, the cell-autonomous electrophysiological disturbances that led us to observe an increase in sEPSC amplitude in *Pten*-Rictor LOF DGCs were not apparent in recordings from CA1 in that model, which could be because of regional differences. For example, if the increase in glutamatergic innervation of the GCL that we observed (Fig. 8) shares some mechanistic similarities with

mossy fiber sprouting, then it is probable that these same mechanisms are not occurring in CA1 or cortical circuits.

The role of aberrant synaptic transmission in *Pten* LOF-induced epilepsy

The present results suggest that aberrant synaptic connectivity and/or transmission, particularly in the dentate GCL, underlie seizures in *Pten* and *Pten*-Rictor LOF animals, possibly by compromising the dentate gyrus gating function (Pun et al., 2012; Krook-Magnuson et al., 2015; Dengler and Coulter, 2016). Furthermore, the aberrant glutamatergic synapses that persist in the GCL in the *Pten*-Rictor LOF mice appear akin to sprouted mossy fibers, which were previously described with PTEN LOF in DGCs, and were thought to be a consequence of seizures (Pun et al., 2012). The potential of these synapses to be like mossy fiber sprouting, however, raises the possibility that some of the synaptic changes we see could be a cause or consequence of epilepsy. Two of our observations, however, suggest that the PTEN LOF-induced synaptic changes not rescued by mTORC2 inactivation are not the consequence of seizures or epileptic activity. First, not all of the *Pten* LOF or *Pten*-Rictor LOF animals in the present study developed spontaneous generalized seizures, at least at a high enough frequency for us to detect. A limitation to this argument is the fact that we did not perform intrahippocampal EEG recording, which can detect focal epileptic events in the dentate gyrus of *Pten* LOF mice (LaSarge et al., 2021). Second, our finding that synaptic changes caused by *Pten* LOF were not prevented with Rictor LOF in the single-neuron culture suggests that the observed synaptic alterations are not dependent on epileptic activity. Synaptic changes in the *Pten*-Rictor LOF neurons were also not limited to those directly caused by *Pten* LOF. The amplitudes of mEPSCs (single neuron recordings) were further increased above *Pten* LOF by *Pten*-Rictor LOF (Fig. 9). *Pten*-Rictor LOF also caused additional presynaptic alterations, such as decreased release probability and increased short-term plasticity (Fig. 10). Previously, we showed that deletion of *Rictor* alone impaired presynaptic function (McCabe et al., 2020). Thus, in addition to not preventing some of the increases in synaptic connectivity caused by *Pten* LOF, mTORC2 inactivation causes *de novo* impairments of synaptic transmission that may further contribute to epileptogenesis.

Our data show that genetic inactivation of mTORC2 does not prevent epileptic activity in the *Gfap-Cre;Pten* model. We were not able to test whether mTORC1 inactivation protected against seizures in this model because of increased mortality of *Pten*-Raptor LOF mice. The fact that neither mTORC1 nor mTORC2 inhibition was beneficial to these mice is somewhat surprising because rapamycin treatment was previously shown to improve seizure phenotypes in the same model (Ljungberg et al., 2009; Sunnen et al., 2011; Nguyen et al., 2015). One possibility for this difference is that simultaneous mTORC1 and mTORC2 inhibition is necessary to prevent epileptogenesis in this model. There is substantial crosstalk between mTORC1 and mTORC2 signaling; thus, inhibiting one arm may further exacerbate signaling abnormalities through the other (Xie and Proud, 2014). Rapamycin treatment may also differ from genetic inactivation in that it does not completely shut down mTORC1 or mTORC2 signaling (Thoreen et al., 2009; Kang et al., 2013), leaving a better window for therapeutic effects.

References

- Anglikar N, Burri M, Zaichuk M, Fritschy JM, Ruegg MA (2015) mTORC1 and mTORC2 have largely distinct functions in Purkinje cells. *Eur J Neurosci* 42:2595–2612.

- Backman SA, Stambolic V, Suzuki A, Haight J, Elia A, Pretorius J, Tsao MS, Shannon P, Bolon B, Ivy Go, Mak TW (2001) Deletion of Pten in mouse brain causes seizures, ataxia and defects in soma size resembling Lhermitte-Duclos disease. *Nat Genet* 29:396–403.
- Barrows CM, McCabe MP, Chen H, Swann JW, Weston MC (2017) PTEN loss increases the connectivity of fast synaptic motifs and functional connectivity in a developing hippocampal network. *J Neurosci* 37:8595–8611.
- Binder MS, Lugo JN (2017) NS-Pten knockout mice show sex- and age-specific differences in ultrasonic vocalizations. *Brain Behav* 7:e00857.
- Burgalossi A, Jung S, Man KN, Nair R, Jockusch WJ, Wojcik SM, Brose N, Rhee JS (2012) Analysis of neurotransmitter release mechanisms by photolysis of caged Ca(2)(+) in an autaptic neuron culture system. *Nat Protoc* 7:1351–1365.
- Casanova E, Fehsenfeld S, Mantamadiotis T, Lemberger T, Greiner E, Stewart AF, Schutz G (2001) A CamKIIalpha iCre BAC allows brain-specific gene inactivation. *Genesis* 31:37–42.
- Chen CJ, Sgritta M, Mays J, Zhou H, Lucero R, Park J, Wang IC, Park JH, Kaiparettu BA, Stoica L, Jafar-Nejad P, Rigo F, Chin J, Noebels JL, Costa-Mattioli M (2019) Therapeutic inhibition of mTORC2 rescues the behavioral and neurophysiological abnormalities associated with Pten deficiency. *Nat Med* 25:1684–1690.
- Costa-Mattioli M, Monteggia LM (2013) mTOR complexes in neurodevelopmental and neuropsychiatric disorders. *Nat Neurosci* 16:1537–1543.
- Crino PB (2016) The mTOR signalling cascade: paving new roads to cure neurological disease. *Nat Rev Neurol* 12:379–392.
- Dengler CG, Coulter DA (2016) Normal and epilepsy-associated pathologic function of the dentate gyrus. *Prog Brain Res* 226:155–178.
- Dragatsis I, Zeitlin S (2000) CamKIIalpha-Cre transgene expression and recombination patterns in the mouse brain. *Genesis* 26:133–135.
- French JA, Lawson JA, Yapici Z, Ikeda H, Polster T, Nabbout R, Curatolo P, De Vries PJ, Dlugos DJ, Berkowitz N, Voi M, Peyrard S, Pelov D, Franz DN (2016) Adjunctive everolimus therapy for treatment-resistant focal-onset seizures associated with tuberous sclerosis (EXIST-3): a phase 3, randomised, double-blind, placebo-controlled study. *Lancet* 388:2153–2163.
- Fricano-Kugler CJ, Williams MR, Salinaro JR, Li M, Luikart B (2016) Designing, packaging, and delivery of high titer CRISPR retro and lentiviruses via stereotaxic injection. *J Vis Exp* 111:53783.
- Fricano CJ, Despenza T Jr, Frazel PW, Li M, O'Malley AJ, Westbrook GL, Luikart BW (2014) Fatty acids increase neuronal hypertrophy of Pten knockdown neurons. *Front Mol Neurosci* 7:30.
- Getz SA, Despenza T Jr, Li M, Luikart BW (2016) Rapamycin prevents, but does not reverse, aberrant migration in Pten knockout neurons. *Neurobiol Dis* 93:12–20.
- Hsieh LS, Wen JH, Claycomb K, Huang Y, Harrsch FA, Naegle JR, Hyder F, Buchanan GF, Bordey A (2016) Convulsive seizures from experimental focal cortical dysplasia occur independently of cell misplacement. *Nat Commun* 7:11753.
- Jansen LA, Mirzaa GM, Ishak GE, O'Roak BJ, Hiatt JB, Roden WH, Gunter SA, Christian SL, Collins S, Adams C, Riviere JB, St-Onge J, Ojemann JG, Shendure J, Hevner RF, Dobyns WB (2015) PI3K/AKT pathway mutations cause a spectrum of brain malformations from megalencephaly to focal cortical dysplasia. *Brain* 138:1613–1628.
- Kang SA, Pacold ME, Cervantes CL, Lim D, Lou HJ, Ottina K, Gray NS, Turk BE, Yaffe MB, Sabatini DM (2013) mTORC1 phosphorylation sites encode their sensitivity to starvation and rapamycin. *Science* 341:1236566.
- Koboldt DC, et al. (2021) PTEN somatic mutations contribute to spectrum of cerebral overgrowth. *Brain* 144:2971–2978.
- Krook-Magnuson E, Armstrong C, Bui A, Lew S, Oijala M, Soltész I (2015) In vivo evaluation of the dentate gate theory in epilepsy. *J Physiol* 593:2379–2388.
- Kwon CH, Zhu X, Zhang J, Knoop LL, Tharp R, Smeyne RJ, Eberhart CG, Burger PC, Baker SJ (2001) Pten regulates neuronal soma size: a mouse model of Lhermitte-Duclos disease. *Nat Genet* 29:404–411.
- Kwon CH, Luikart BW, Powell CM, Zhou J, Matheny SA, Zhang W, Li Y, Baker SJ, Parada LF (2006) Pten regulates neuronal arborization and social interaction in mice. *Neuron* 50:377–388.
- Lamming DW, Ye L, Katajisto P, Goncalves MD, Saitoh M, Stevens DM, Davis JG, Salmon AB, Richardson A, Ahima RS, Guertin DA, Sabatini DM, Baur JA (2012) Rapamycin-induced insulin resistance is mediated by mTORC2 loss and uncoupled from longevity. *Science* 335:1638–1643.
- Laplante M, Sabatini DM (2012) mTOR signaling in growth control and disease. *Cell* 149:274–293.
- LaSarge CL, Danzer SC (2014) Mechanisms regulating neuronal excitability and seizure development following mTOR pathway hyperactivation. *Front Mol Neurosci* 7:18.
- LaSarge CL, Pun RY, Muntifering MB, Danzer SC (2016) Disrupted hippocampal network physiology following PTEN deletion from newborn dentate granule cells. *Neurobiol Dis* 96:105–114.
- LaSarge CL, Pun RY, Gu Z, Riccetti MR, Namboodiri DV, Tiwari D, Gross C, Danzer SC (2021) mTOR-driven neural circuit changes initiate an epileptogenic cascade. *Prog Neurobiol* 200:101974.
- Lipton JO, Sahin M (2014) The neurology of mTOR. *Neuron* 84:275–291.
- Liu GY, Sabatini DM (2020) mTOR at the nexus of nutrition, growth, ageing and disease. *Nat Rev Mol Cell Biol* 21:183–203.
- Ljungberg MC, Sunnen CN, Lugo JN, Anderson AE, D'Arcangelo G (2009) Rapamycin suppresses seizures and neuronal hypertrophy in a mouse model of cortical dysplasia. *Dis Model Mech* 2:389–398.
- Lugo JN, Smith GD, Morrison JB, White J (2013) Deletion of PTEN produces deficits in conditioned fear and increases fragile X mental retardation protein. *Learn Mem* 20:670–673.
- Lugo JN, Smith GD, Ar buckle EP, White J, Holley AJ, Floruta CM, Ahmed N, Gomez MC, Okonkwo O (2014) Deletion of PTEN produces autism-like behavioral deficits and alterations in synaptic proteins. *Front Mol Neurosci* 7:27.
- Luikart BW, Bensen AL, Washburn EK, Perederiy JV, Su KG, Li Y, Kernie SG, Parada LF, Westbrook GL (2011a) miR-132 mediates the integration of newborn neurons into the adult dentate gyrus. *PLoS One* 6:e19077.
- Luikart BW, Schnell E, Washburn EK, Bensen AL, Tovar KR, Westbrook GL (2011b) Pten knockdown *in vivo* increases excitatory drive onto dentate granule cells. *J Neurosci* 31:4345–4354.
- Marchese M, Conti V, Valvo G, Moro F, Muratori F, Tancredi R, Santorelli FM, Guerrini R, Sicca F (2014) Autism-epilepsy phenotype with macrocephaly suggests PTEN, but not GLIALCAM, genetic screening. *BMC Med Genet* 15:26.
- Matsushita Y, Sakai Y, Shimmura M, Shigeto H, Nishio M, Akamine S, Saneuji M, Ishizaki Y, Torisu H, Nakabeppu Y, Suzuki A, Takada H, Hara T (2016) Hyperactive mTOR signals in the proopiomelanocortin-expressing hippocampal neurons cause age-dependent epilepsy and premature death in mice. *Sci Rep* 6:22991.
- McCabe MP, Cullen ER, Barrows CM, Shore AN, Tooke KI, Laprade KA, Stafford JM, Weston MC (2020) Genetic inactivation of mTORC1 or mTORC2 in neurons reveals distinct functions in glutamatergic synaptic transmission. *Elife* 9:e51440.
- McCabe MP, Shore AN, Frankel WN, Weston MC (2021) Altered fast synaptic transmission in a mouse model of DNMT1-associated developmental epileptic encephalopathy. *eNeuro* 8:ENEURO.0269-20.2020.
- McMahon J, Huang X, Yang J, Komatsu M, Yue Z, Qian J, Zhu X, Huang Y (2012) Impaired autophagy in neurons after disinhibition of mammalian target of rapamycin and its contribution to epileptogenesis. *J Neurosci* 32:15704–15714.
- Moen EL, Fricano-Kugler CJ, Luikart BW, O'Malley A (2016) Analyzing clustered data: why and how to account for multiple observations nested within a study participant? *PLoS One* 11:e0146721.
- Moloney PB, Cavalleri GL, Delanty N (2021) Epilepsy in the mTORopathies: opportunities for precision medicine. *Brain Commun* 3:fcab222.
- Nguyen LH, Bordey A (2021) Convergent and divergent mechanisms of epileptogenesis in mTORopathies. *Front Neuroanat* 15:664695.
- Nguyen LH, Brewster AL, Clark ME, Regnier-Golanov A, Sunnen CN, Patil VV, D'Arcangelo G, Anderson A (2015) mTOR inhibition suppresses established epilepsy in a mouse model of cortical dysplasia. *Epilepsia* 56:636–646.
- Nguyen LH, Xu Y, Mahadeo T, Zhang L, Lin TV, Born HA, Anderson AE, Bordey A (2022) Expression of 4E-BP1 in juvenile mice alleviates mTOR-induced neuronal dysfunction and epilepsy. *Brain* 145:1310–1325.
- Proietti Onori M, Koene LM, Schafer CB, Nellist M, de Brito Van Velze M, Gao Z, Elgersma Y, Van Woerden GM (2021) RHEB/mTOR hyperactivity causes cortical malformations and epileptic seizures through increased axonal connectivity. *PLoS Biol* 19:e3001279.
- Pun RY, Rolle IJ, Lasarge CL, Hosford BE, Rosen JM, Uhl JD, Schmeltzer SN, Faulkner C, Bronson SL, Murphy BL, Richards DA, Holland KD, Danzer SC (2012) Excessive activation of mTOR in postnatally generated granule cells is sufficient to cause epilepsy. *Neuron* 75:1022–1034.

- Rodriguez A, Ehlenberger DB, Dickstein DL, Hof PR, Wearne SL (2008) Automated three-dimensional detection and shape classification of dendritic spines from fluorescence microscopy images. *PLoS One* 3:e1997.
- Santos VR, Pun RY, Arafat SR, Lasarge CL, Rowley S, Khademi S, Bouley T, Holland KD, Garcia-Cairasco N, Danzer SC (2017) PTEN deletion increases hippocampal granule cell excitability in male and female mice. *Neurobiol Dis* 108:339–351.
- Sarbassov DD, Ali SM, Sengupta S, Sheen JH, Hsu PP, Bagley AF, Markhard AL, Sabatini DM (2006) Prolonged rapamycin treatment inhibits mTORC2 assembly and Akt/PKB. *Mol Cell* 22:159–168.
- Sarbassov DD, Guertin DA, Ali SM, Sabatini DM (2005) Phosphorylation and regulation of Akt/PKB by the Rictor-mTOR complex. *Science* 307:1098–1101.
- Skelton PD, Poquerusse J, Salinaro JR, Li M, Luikart BW (2020) Activity-dependent dendritic elaboration requires Pten. *Neurobiol Dis* 134:104703.
- Srivastava S, Jo B, Zhang B, Frazier T, Gallagher AS, Peck F, Levin AR, Mondal S, Li Z, Filip-Dhima R, Geisel G, Dies KA, Diplock A, Eng C, Hanna R, Sahin M, Hardan A (2022) A randomized controlled trial of Everolimus for neurocognitive symptoms in PTEN hamartoma tumor syndrome. *Hum Mol Genet* 31:3393–3404.
- Sunnen CN, Brewster AL, Lugo JN, Vanegas F, Turcios E, Mukhi S, Parghi D, D'Arcangelo G, Anderson AE (2011) Inhibition of the mammalian target of rapamycin blocks epilepsy progression in NS-Pten conditional knockout mice. *Epilepsia* 52:2065–2075.
- Thoreen CC, Kang SA, Chang JW, Liu Q, Zhang J, Gao Y, Reichling LJ, Sim T, Sabatini DM, Gray NS (2009) An ATP-competitive mammalian target of rapamycin inhibitor reveals rapamycin-resistant functions of mTORC1. *J Biol Chem* 284:8023–8032.
- Tsien JZ, Chen DF, Gerber D, Tom C, Mercer EH, Anderson DJ, Mayford M, Kandel ER, Tonegawa S (1996) Subregion- and cell type-restricted gene knockout in mouse brain. *Cell* 87:1317–1326.
- Vogt D, Cho KK, Lee AT, Sohal VS, Rubenstein JL (2015) The parvalbumin/somatostatin ratio is increased in Pten mutant mice and by human PTEN ASD alleles. *Cell Rep* 11:944–956.
- Weston MC, Chen H, Swann JW (2012) Multiple roles for mammalian target of rapamycin signaling in both glutamatergic and GABAergic synaptic transmission. *J Neurosci* 32:11441–11452.
- Weston MC, Chen H, Swann JW (2014) Loss of mTOR repressors Tsc1 or Pten has divergent effects on excitatory and inhibitory synaptic transmission in single hippocampal neuron cultures. *Front Mol Neurosci* 7:1.
- Williams MR, Despenza T Jr, Li M, Gullledge AT, Luikart BW (2015) Hyperactivity of newborn Pten knock-out neurons results from increased excitatory synaptic drive. *J Neurosci* 35:943–959.
- Winden KD, Ebrahimi-Fakhari D, Sahin M (2018) Abnormal mTOR activation in autism. *Annu Rev Neurosci* 41:1–23.
- Wong M (2013) Mammalian target of rapamycin (mTOR) pathways in neurological diseases. *Biomed J* 36:40–50.
- Xie J, Proud CG (2014) Signaling crosstalk between the mTOR complexes. *Translation (Austin)* 2:e28174.
- Xiong Q, Oviedo HV, Trotman LC, Zador AM (2012) PTEN regulation of local and long-range connections in mouse auditory cortex. *J Neurosci* 32:1643–1652.
- Zhang L, Huang T, Teaw S, Nguyen LH, Hsieh LS, Gong X, Burns LH, Bordey A (2020) Filamin A inhibition reduces seizure activity in a mouse model of focal cortical malformations. *Sci Transl Med* 12:eaay0289.
- Zhou J, Blundell J, Ogawa S, Kwon CH, Zhang W, Sinton C, Powell CM, Parada LF (2009) Pharmacological inhibition of mTORC1 suppresses anatomical, cellular, and behavioral abnormalities in neural-specific Pten knock-out mice. *J Neurosci* 29:1773–1783.